Published in final edited form as:

Neuron. 2021 January 20; 109(2): 314–330.e4. doi:10.1016/j.neuron.2020.10.031.

Mediodorsal and ventromedial thalamus engage distinct L1 circuits in the prefrontal cortex

Paul G. Anastasiades[1,2,3], **David P. Collins**[1,2], **Adam G. Carter**[2,*]

[1]These authors contributed equally

[2]Center for Neural Science, New York University, 4 Washington Place, New York, NY 10003, USA

[3]Present address: Department of Translational Health Sciences, University of Bristol, Dorothy Hodgkin Building, Whitson Street, Bristol, BS1 3NY, UK

SUMMARY

Interactions between the thalamus and prefrontal cortex (PFC) play a critical role in cognitive function and arousal. Here we use anatomical tracing, electrophysiology, optogenetics, and 2-photon Ca2+ imaging to determine how ventromedial (VM) and mediodorsal (MD) thalamus target specific cell types and subcellular compartments in layer 1 (L1) of mouse PFC. We find thalamic inputs make distinct connections in L1, where VM engages NDNF+ cells in L1a, and MD drives VIP+ cells in L1b. These separate populations of L1 interneurons participate in different inhibitory networks in superficial layers by targeting either PV+ or SOM+ interneurons. NDNF+ cells also inhibit the apical dendrites of L5 pyramidal tract (PT) cells to suppress AP-evoked Ca2+ signals. Lastly, NDNF+ cells mediate a unique form of thalamus-evoked inhibition at PT cells, selectively blocking VM-evoked dendritic Ca2+ spikes. Together, our findings reveal how two thalamic nuclei differentially communicate with the PFC through distinct L1 micro-circuits.

eTOC

Anastasiades et al. show how VM and MD thalamus differentially engage NDNF and VIP interneurons located in L1 of the mouse prefrontal cortex. These interneurons participate in distinct inhibitory and disinhibitory micro-circuits, with feed-forward inhibition via NDNF interneurons regulating VM-evoked Ca2+ signals in the apical dendrites of L5 pyramidal cells.

*Corresponding author & lead contact: adam.carter@nyu.edu.

AUTHOR CONTRIBUTIONS

Conceptualization, A.G.C., P.G.A. and D.P.C.; Investigation, P.G.A. and D.P.C.; Writing, A.G.C., P.G.A. and D.P.C.; Supervision, A.G.C.; Funding Acquisition, A.G.C.

DECLARATION OF INTERESTS

The authors have no financial conflicts of interest.

INTRODUCTION

Communication between the thalamus and prefrontal cortex (PFC) is critical for cognition and disrupted in mental health disorders (Huang et al., 2019; Ouhaz et al., 2018; Pergola et al., 2018). The PFC engages several higher-order nuclei, including reciprocal interactions with mediodorsal (MD) and ventromedial (VM) thalamus (Collins et al., 2018; Gabbott et al., 2005). While the behavioral and computational roles of these nuclei have not been fully elucidated, connections with MD sustain delay period activity during working memory (Bolkan et al., 2017; Schmitt et al., 2017), whereas those with VM regulate arousal (Honjoh et al., 2018). The behavioral roles of these nuclei likely reflect their impact on different circuits within the PFC, with MD inputs driving layer 2/3 (L2/3) pyramidal cells, and VM synapsing onto but not firing L2/3 and L5 pyramidal cells (Collins et al., 2018). Interestingly, both MD and VM inputs also project to L1, but it remains unclear how these connections contribute to their functional influence on the PFC.

Both MD and VM elicit robust inhibition in the PFC (Collins et al., 2018), which can be mediated by a variety of GABAergic interneurons. MD targets parvalbumin-positive (PV+) cells in L2/3 (Delevich et al., 2015), but targeting of L1 interneurons is unknown. In contrast, VM engages L1 interneurons (Cruikshank et al., 2012), which have diverse properties (Chu et al., 2003; Jiang et al., 2013; Lee et al., 2013; Schuman et al., 2019; Wozny and Williams, 2011; Zhou and Hablitz, 1996). L1 interneurons express 5HT3a receptors (5HT3aR+) (Rudy et al., 2011), and are further classified by the expression of either vasoactive intestinal peptide (VIP+) or neuron derived neurotrophic factor (NDNF+) (Schuman et al., 2019). Throughout the cortex, VIP+ cells typically target somatostatin (SOM+) cells to mediate disinhibition (Lee et al., 2013; Pfeffer et al., 2013; Pi et al., 2013). In contrast, NDNF+ cells are less understood, but appear to be neurogliaform cells (Schuman et al., 2019) that can inhibit pyramidal cell dendrites (Abs et al., 2018). By targeting either VIP+ or NDNF+ cells, MD and VM could either inhibit or disinhibit the PFC, with important implications for network activity (Letzkus et al., 2011; Palmer et al., 2012; Pi et al., 2013).

Thalamic inputs to L1 are also well positioned to contact the apical dendrites of pyramidal cells residing in deeper layers (Rubio-Garrido et al., 2009). Recent studies from frontal cortex show VM innervation is localized to the apical dendrites of pyramidal tract (PT) cells in L5 (Collins et al., 2018; Guo et al., 2018). While these inputs do not appear to drive somatic firing (Collins et al., 2018), they may generate dendritic Ca2+ spikes (Zhu and Connors, 1999). Interestingly, dendritic Ca2+ signals are tightly regulated by GABAergic inhibition via SOM+ and 5HT3aR+ interneurons (Chalifoux and Carter, 2011; Chiu et al., 2013; Marlin and Carter, 2014; Palmer et al., 2012; Pérez-Garci et al., 2006). If VM inputs engage a subset of 5HT3aR+ cells, they could also mediate a local feed-forward inhibitory circuit within L1. Because PT cells project back to thalamus (Harris and Shepherd, 2015), this local inhibition could influence cortico-thalamocortical loops that are critical for PFC-dependent behaviors (Bolkan et al., 2017; Guo et al., 2017; Schmitt et al., 2017).

Here we combine anatomical tracing, electrophysiology, optogenetics, 2-photon Ca2+ imaging, and pharmacology to dissect how higher-order thalamic inputs from MD and VM

engage multiple circuits in the superficial layers of the prelimbic PFC. We first show that L1 consists of two sublayers, with VM selectively driving NDNF+ cells in L1a, and MD engaging VIP+ cells in L1b. We then show that these interneurons participate in distinct inhibitory networks, with NDNF+ cells inhibiting PV+ cells and VIP+ cells inhibiting SOM + cells in L2/3. We also show that NDNF+ cells inhibit the apical dendrites of pyramidal cells, suppressing action potential (AP)-evoked Ca2+ signals in the distal dendrites of PT cells in L5. Lastly, we show that NDNF+ cells mediate thalamus-evoked inhibition, blocking VM-evoked Ca2+ signals in the apical dendrites of PT cells. Together, our findings reveal tab differences between two higher-order thalamic inputs to PFC, highlighting how they target distinct networks of L1 interneurons, and suggesting novel roles for both VM inputs and NDNF+ cells in gating communication between the cortex and thalamus.

RESULTS

Thalamic inputs and GABAergic interneurons distinguish sublayers of L1

Both VM and MD thalamus innervate L1 of the prelimbic PFC, but how they influence local micro-circuits remains unclear. To explore these connections, we co-injected AAVs expressing EGFP or mCherry into VM and MD (n = 3 mice each) (Fig. 1A). We found both afferents densely innervated L1 of the prelimbic cortex, with VM axon prominent in the outer half (L1a), and MD axon greater in the inner half (L1b) (peak axon density (% L1 depth): MD = 45.7 ± 1.3%, VM = 9.3 ± 1.6%) (Fig. 1B & Fig. S1) and a second band of MD axon in L3 (Fig. S1) (Collins et al., 2018). The spatial separation of these axon arborizations suggested that VM and MD may have different postsynaptic targets within L1. Several classes of GABAergic interneurons are found in L1, with the main subtypes being NDNF+ and VIP+ cells (Schuman et al., 2019). We examined the distributions of these cells by injecting AAV-FLEX-EGFP or AAV-FLEX-tdTomato into the PFC of 5HT3aR-Cre, NDNF-Cre or VIP-Cre mice (n = 3 mice each) (Fig. 1C). We found that 5HT3aR+ cells spanned L1, whereas NDNF+ cells were biased towards L1a and VIP+ cells were restricted to L1b (Fig. 1D), indicating that these cell types are also spatially segregated.

To characterize the properties of L1 interneurons in the prelimbic PFC, we next made whole-cell recordings from *ex vivo* slices. We found VIP+ cells in L1b had bitufted or bipolar morphologies, along with non-fast-spiking (NFS), irregular-spiking (IS), or fast-adapting (fAD) firing properties (n = 17 VIP+ cells, 8 mice; NFS = 9/17, IS = 5/17, fAD = 3/17) (Fig. 1E–G & Fig. S1). In contrast, NDNF+ cells in L1a had horizontal morphologies and late-spiking (LS) firing properties (n = 12 NDNF+ cells, 4 mice; LS = 11/12, non-LS = 1/12) (Fig. 1E–G & Fig. S1), with a slow ramp-to-spike at near-threshold potentials (Chu et al., 2003; Schuman et al., 2019). VIP− cells in L1a of VIP-Cre × Ai14 mice had indistinguishable properties to NDNF+ cells (n = 17 cells, 8 mice) (Fig. 1E–G & Fig. S1). Hierarchical cluster analysis of intrinsic properties supported the presence of two groups, one dominated by VIP+ cells and the other by NDNF+ and VIP− cells (Fig. S1). These results show that NDNF+ and VIP+ cells have distinct morphological and physiological properties and segregate into separate sublayers, indicating the two main classes of L1 interneurons may differentially receive and process MD and VM inputs, suggesting complementary activation of superficial networks.

Brain-wide retrograde tracing indicates differential interneuron innervation

The distributions of VIP+ and NDNF+ cells in L1 indicated they may receive and process different local and long-range inputs. To map their brain-wide innervation, we performed monosynaptic input tracing using a conditional rabies virus approach (Wall et al., 2010). We first injected AAV-FLEX-TVA-mCherry and AAV-FLEX-oG into the PFC of either NDNF-Cre or VIP-Cre mice (Fig. 2A). After allowing for expression, we then injected SADΔG-GFP (EnvA) pseudotyped rabies virus to infect Cre+ interneurons. Starter cells were primarily located in prelimbic PFC (Fig. 2A & Fig. S2), with GFP+ monosynaptic input neurons found in all layers of the local circuit (Fig. 2B). We also observed GFP+ cells across the rostral-caudal axis of the brain (VIP-Cre: n = 23,483 cells, 5 mice; NDNF-Cre: n = 21,448 cells, 3 mice) (Fig. 2C & Fig. S2). The main extra-cortical input was thalamus, in addition to striatum and pallidum, hippocampus, amygdala, claustrum, olfactory regions, hypothalamus and various midbrain and hindbrain structures (Fig. 2D & Figs. S2 & S3; Supp. Tables 1 & 2). VIP+ cells received a greater proportion of input from prefrontal regions, although no specific subregion accounted for this bias (Fig. S3). In contrast, NDNF + cells received greater subcortical input from cholinergic areas, suggesting they may be differentially modulated (Fig. S2). Thalamic input to both interneuron populations came mostly from higher-order / secondary nuclei (VIP+ = 81.7 ± 1.2%, NDNF+ = 79.5 ± 2.2%) (Fig. S3) (Phillips et al., 2019). However, we observed major differences in the relative composition of this input, with VIP+ cells receiving a greater proportion of input from MD (VIP+ = 36.0 ± 1.2%, NDNF+ = 17.3 ± 0.6%, $p < 0.0001$), and NDNF+ cells from VM (VIP + = 14.3 ± 1.6%, NDNF+ = 23.8 ± 4.5%, $p = 0.0004$) (Fig. 2E–F). This difference was highlighted by the MD / VM ratio for input to VIP+ and NDNF+ starter cells (VIP+ = 2.6, CI = 1.8–3.8; NDNF+ = 0.8, CI = 0.4–1.5; VIP+ vs. NDNF+, $p = 0.036$) (Fig. 2G). Together, these findings indicate both interneuron subtypes receive considerable brain-wide input but suggest differential thalamic targeting by MD and VM.

MD and VM innervate and activate different subtypes of L1 interneurons

While rabies tracing provides clues about differences in connectivity, it cannot reveal the strength or dynamics of synapses. To understand how VM and MD engage L1 micro-circuits, we next injected AAV-ChR2-EYFP into VM or MD of VIP-Cre × Ai14 mice and made whole-cell recordings from VIP+ cells in L1b and VIP− cells in L1a (equivalent to NDNF+ cells) (Fig. 3A). Because VIP− cells in L1a are physiologically and morphologically indistinguishable from NDNF+ cells, this approach allows us to compare the activation of the two main types of L1 interneurons in the same slice. Trains of VM inputs (5 pulses @ 10 Hz with a 473 nm LED) elicited robust EPSCs at VIP− cells in L1a, which were much stronger than those at VIP+ cells in L1b (VIP− = −146 ± 41 pA, VIP+ = −6 ± 2 pA, $p = 0.016$; n = 7 pairs, 5 mice) (Fig. 3A–B). In contrast, we found comparable MD-evoked EPSC amplitudes at each cell type (VIP− = −57 ± 22 pA, VIP+ = −41 ± 13 pA, $p = 0.68$; n = 7 pairs, 5 mice) (Fig. 3A–B). This differential thalamic targeting of L1 interneurons was highlighted by VIP− / VIP+ input ratios, which were close to unity for MD, but an order of magnitude higher for VM (MD = 0.94, CI = −0.03–3.4, $p = 0.58$; VM = 25.9, CI = 8.4–82.6, $p = 0.016$; MD vs. VM, $p = 0.001$) (Fig. 3C). Interestingly, both MD and VM inputs to VIP+ cells showed facilitation, while VIP− cells displayed initial facilitation followed by depression (Fig. 3D). These results indicate that thalamic inputs

differentially engage L1 interneurons, with VM stronger onto VIP− cells, and MD showing no bias. They also show how differences in synapse strength depend on the source of thalamic input, whereas short-term dynamics depend on the post-synaptic cell type.

To determine how differences in connectivity impact action potential (AP) firing, we performed separate current-clamp experiments. VM inputs drove robust AP firing of VIP− cells in L1a, with minimal activation of VIP+ cells in L1b (Fig. 3E–G; VIP− p-spike = 0.88 ± 0.07, VIP+ p-spike = 0.14 ± 0.14, p = 0.03; n = 7 pairs, 4 mice). In contrast, MD input activated VIP+ cells in L1b more strongly than VIP− cells in L1a (Fig. 3E–G; VIP− p-spike = 0.33 ± 0.13, VIP+ p-spike = 0.81 ± 0.10, p = 0.04; n = 8 pairs, 5 mice). This reflects the intrinsic properties of VIP+ cells, which are much more excitable than NDNF+ / VIP− cells (Fig. 1G). Together, these findings indicate that L1 contains two distinct inhibitory micro-circuits, one mediated by NDNF+ interneurons in L1a and strongly activated by VM, the other by VIP+ interneurons in L1b and driven by MD.

VIP+ and NDNF+ interneurons participate in distinct output pathways

Having determined how MD and VM engage L1 interneurons, we next examined how these cells in turn engage the local network. The axonal projections of VIP+ and NDNF+ interneurons suggested that they may target distinct postsynaptic cells. To test this idea, we crossed VIP-Cre or NDNF-Cre mice with either G42 or GIN reporter mice, which label subsets of PV+ and SOM+ interneurons, respectively (Chattopadhyaya et al., 2004; Oliva et al., 2000), allowing us to distinguish them from unlabeled L2/3 pyramidal cells (PYRs) (Fig. S4). We then injected AAV-DIO-ChR2-mCherry into the PFC and recorded light-evoked IPSCs from L2/3 interneurons or PYRs in the presence of TTX and 4-AP (Anastasiades et al., 2018a; Petreanu et al., 2009) (Fig. 4A–B). For VIP-evoked IPSCs, we found large responses at SOM+ interneurons, but neither PYR nor PV+ cells (PYR = 21 ± 7 pA, n = 10 cells, 7 mice; PV+ = 28 ± 9 pA, n = 9 cells, 6 mice; SOM+ = 342 ± 77 pA, n = 10 cells, 5 mice; SOM+ vs. PYR, p = <0.0001; SOM+ vs. PV+ p = 0.0003) (Fig. 4A,C). For NDNF-evoked IPSCs, we found the opposite relationship, with large responses at PYR and PV+ cells, but not SOM+ cells (PYR = 88.5 ± 21 pA, n = 14 cells, 5 mice; PV+ = 56 ± 16 pA, n = 10 cells, 5 mice; SOM+ = 10 ± 6 pA, n = 8 cells, 4 mice; SOM vs. PYR, p = 0.0004; SOM vs. PV, p = 0.0085) (Fig. 4B–C). These findings indicate that NDNF+ and VIP+ interneurons participate in distinct micro-circuits in superficial layers of the PFC, potentially engaging different disinhibitory pathways via SOM+ and PV+ interneurons, respectively.

In other cortices, L1 neurogliaform cells, which are a subset of NDNF+ interneurons, evoke inhibitory responses via slow $GABA_A$ and $GABA_B$ receptors (Oláh et al., 2007, 2009). Consistent with this idea, we found NDNF-evoked IPSCs were markedly slower than VIP-evoked IPSCs (Fig. 4D & Fig. S4). To further examine connections onto PV+ and PYR cells in the PFC, we also performed a separate set of current-clamp recordings, using selective pharmacology to assay the involvement of ionotropic and metabotropic receptors. Both PYR and PV+ cells had biphasic IPSPs (Fig. 4E & Fig. S4) (NDNF+ → PYR: n = 5 cells, 2 mice; NDNF+ → PV+: n = 5 cells, 4 mice), with a slow component sensitive to the $GABA_B$-R antagonist CGP (2 μM) and fast component blocked by the $GABA_A$-R antagonist gabazine (GZ; 10 μM) (Fig. 4E–F & Fig. S4). In contrast, VIP+ → SOM+ connections did not reveal

any $GABA_B$-mediated IPSP (Fig. 4E–F) (VIP+ → SOM+: n = 7 cells, 3 mice). These findings indicate that NDNF+ cells engage slow inhibition via $GABA_B$ receptors, and fast inhibition via $GABA_A$ receptors. The latter component suggests a role for NDNF+ cells in rapid, thalamus-evoked feed-forward inhibition at PFC pyramidal neurons.

Differential innervation of PT and IT cells by NDNF+ interneurons

Our results show that NDNF+ cells synapse onto pyramidal cells, suggesting they play a role in thalamus-evoked feed-forward inhibition. Because their axons extend across L1, NDNF+ cells may also target the dendrites of pyramidal cells residing in deeper layers (Abs et al., 2018; Jiang et al., 2013; Zhou and Hablitz, 1996). L5 pyramidal cells segregate into pyramidal tract (PT) and intratelencephalic (IT) cells, which possess distinct properties (Harris and Shepherd, 2015). For example, the strength of excitatory inputs from thalamus and inhibitory inputs from PV+ and SOM+ cells differ at PT and IT cells (Anastasiades et al., 2018a; Collins et al., 2018; Hilscher et al., 2017). To test if this is also true for connections from NDNF+ cells, we applied widefield optogenetic stimulation of NDNF+ cells and recorded from triplets of retrogradely-labeled PT and IT cells, as well as unlabeled PYR cells in L2/3 (Fig. 5A). Calculating the pairwise ratio of IPSC amplitudes for PT / PYR and PT / IT cells, we found that NDNF-evoked IPSCs were larger at PT cells than IT cells, with no difference between PT and PYR cells (PT / PYR ratio = 1.5, CI = 0.5–2.5, p = 0.64; PT / IT ratio = 2.4, CI = 1.5–3.3, p = 0.016; n = 8 triplets, 3 mice) (Fig. 5A–B & Fig. S5). These findings indicate that NDNF+ cells synapse onto a variety of pyramidal cells, making particularly strong connections onto PT cells.

While these experiments indicate connection strength, they do not reveal the location of presynaptic cells. To confirm that presynaptic neurons were found in L1, we also performed local circuit mapping with soma-restricted optogenetics (Baker et al., 2016; Mardinly et al., 2018). In control experiments, we first confirmed that our stimulation parameters allowed reliable, spatially restricted firing in st-ChroME expressing interneurons (Fig. 5C & S5C). We then assessed connections from NDNF+ cells to PT cells, which represent their strongest outputs in the local micro-circuit. We found that PT cells received pronounced inputs from NDNF+ cells located in L1, with markedly less input from L2/3 and L5 (n = 10 cells, 3 mice) (Fig. 5D–E). In contrast, L2/3 SOM+ cells received VIP+ input from both L1b and superficial L2/3 (n = 12 cells, 6 mice) (Fig. 5E & Fig. S5). Consistent with the sub-laminar distribution of NDNF+ and VIP+ cells in L1a and L1b, the ratio of L1a / L1b input was also higher for NDNF+ connections than VIP+ connections (NDNF+ → PT = 0.8, CI = 0.65–0.94; VIP+ → SOM+ = 0.5, CI = 0.42–0.66; p = 0.016) (Fig. 5F). Together, these findings establish that NDNF+ cells residing in L1 strongly inhibit PT cells.

NDNF+ cells mediate inhibitory control over pyramidal cell apical dendrites

NDNF+ axons are particularly dense in L1, suggesting they may selectively innervate the distal apical dendrites of L5 pyramidal cells. The dendrites of PT and IT cells differ in complexity, with the more extensive arbors of the former potentially enabling more connections (Fig. 6A, Fig. S6). To assess the dendritic location of NDNF+ synapses at pyramidal cells, we performed subcellular ChR2-assisted circuit mapping (sCRACM) in the presence of TTX (1 μM) and 4-AP (0.1 mM) (Petreanu et al., 2009). We found NDNF-

evoked IPSCs were biased onto the distal apical dendrites of PT cells (n = 7 cells, 3 mice) (Fig. 6B–C). Similar targeting was also observed at IT cells (n = 8 cells, 3 mice) (Fig. 6C & S6), suggesting that NDNF+ cells may play an important role in inhibiting apical dendrites.

To assess the influence of this targeting, we used high frequency bursts of APs, which back-propagate into the dendrites to engage voltage-gated ion channels and generate dendritic Ca2+ signals (Larkum et al., 1999; Stuart and Sakmann, 1994; Stuart et al., 1997). Interneurons can strongly inhibit these Ca2+ signals (Chiu et al., 2013; Marlin and Carter, 2014; Palmer et al., 2012; Pérez-Garci et al., 2006), suggesting NDNF+ cells may also perform this role. To test this idea, we recorded in current-clamp from identified PT cells, filling them with the Ca2+ indicator Fluo-5F (0.5 mM) (Fig. 6D) (Chalifoux and Carter, 2011). High frequency trains of APs (3 APs @ 100 Hz) evoked an afterdepolarization (ADP) measured at the soma, which are correlated with dendritic Ca2+ signals (Larkum et al., 1999), which we confirmed by recording simultaneous Ca2+ signals in the distal apical and basal dendrites (Fig. 6D–E). In inter-leaved trials, we activated NDNF+ inputs with 1-photon optogenetics while imaging Ca2+ with 2-photon microscopy. We found NDNF+ inputs to the apical dendrites significantly reduced the ADP (fraction of baseline: apical = 0.69 ± 0.05, p = 0.0156; basal = 0.89 ± 0.05, p = 0.0625) (n = 6 cells, 5 mice) (Fig. 6D) and completely blocked Ca2+ signals (fraction of baseline: apical = 0.09 ± 0.04, p = 0.0156; basal = 0.98 ± 0.05, p = 0.8438) (Fig. 6E). However, NDNF+ inputs to the basal dendrites or apical obliques had minimal influence on either the ADP or Ca2+ signals (Fig. 6D–E & Fig. S6). Similar results were observed in IT cells (n = 8 cells, 6 mice) (Fig. 6D–E & Fig. S6), consistent with similarly prominent NDNF+ inputs to their apical dendrites. These experiments indicate that NDNF+ synapses are enriched at the apical dendrites of PT cells, where they strongly inhibit electrogenesis and Ca2+ signals.

Selective thalamic input onto the apical dendrites of L5 pyramidal cells

In addition to receiving NDNF+ inputs, the elaborate apical dendrites of PT cells are poised to receive VM inputs (Collins et al., 2018). Indeed, equivalent sCRACM analysis of VM input to these cells in the presence of TTX and 4-AP also revealed a strong bias towards the distal apical dendrites that sample L1 (n = 12 cells, 5 mice) (Fig. 7A). Importantly, this targeting greatly differed from IT cells, which received VM input to both the apical and basal dendrites (n = 14 cells, 5 mice) (Fig. 7B & Fig. S7). To determine if this difference reflected stronger synapses on the apical dendrites of PT cells, we compared VM responses at neighboring pairs of L5 cells. Subtracting IT maps from PT maps confirmed VM inputs were stronger at the apical dendrites of PT cells (L1a PT input = −71 ± 9 pA / pixel, L1a IT input = −21 ± 3 pA / pixel, p = 0.0005; L1b PT input = −40 ± 9 pA / pixel, L1b IT input = −12 ± 2 pA / pixel, p = 0.0005; n = 12 pairs) (Fig. 7C & Fig. S7). In contrast, VM input to the basal dendrites was larger at IT cells (L5 PT input = −9 ± 1 pA / pixel, L5 IT input = −27 ± 10 pA / pixel, p = 0.034) (Fig. 7C & Fig. S7). These findings indicate that VM inputs make distinct subcellular connections onto the dendrites of PT and IT cells.

By targeting the distal apical dendrites of PT cells, VM inputs may generate local electrogenic and Ca2+ signals. To test this idea, we next combined whole-cell recordings, optogenetics and 2-photon Ca2+ imaging (Fig. 7D). We found that VM stimulation over the

apical dendrites of PT cells evoked both subthreshold somatic EPSPs (5.82 ± 1.09 mV; n= 12 cells, 10 mice) and Ca2+ signals in apical dendrites and spines (0.043 ± 0.01 $\Delta G/G_{sat}$) (Fig. 7D,F). Consistent with the enrichment of VM input to the apical dendrites, Ca2+ signals were absent from the basal dendrites (Fig. 7D,F). Furthermore, Ca2+ signals were much smaller in both the apical and basal dendrites of IT cells (n = 9 cells, 7 mice) (Fig. 7E,F). Importantly, simultaneous recordings from PYRs remained subthreshold, indicating these findings are not due to recurrent network activity, which would otherwise complicate our interpretation (Fig. S7). Moreover, responses in PYRs were similar across recordings sessions for PT and IT cells, indicating results are not due to differences in the strength of stimulation between experiments (Fig. S7). Instead, these findings indicate a unique functional role for VM input onto the distal apical dendrites of PT cells.

Dendritic excitation-inhibition balance shapes PT cell activation

Our results indicate that VM activates the apical dendrites of PT cells, but also engages NDNF+ cells that inhibit the same dendrites. To assess this feed-forward inhibition, we used dual-color optogenetics (Delevich et al., 2015), activating VM axons with or without suppression of NDNF+ cells. We injected AAV-ChR2 into VM, the fluorescently labeled retrograde tracer Cholera Toxin subunit B (CTB) into PAG, and AAV-FLEX-ArchT (Chow et al., 2010; Han et al., 2011) into PFC of NDNF-Cre mice (Fig. 8A). Recording from NDNF+ cells, we found yellow light (590 nm for 200 ms) activated ArchT to cause a hyperpolarization that silenced APs evoked by either current injection or activation of VM inputs with blue light (473 nm) (Fig. 8B). Recording from PT cells, we observed VM-evoked EPSCs and IPSCs (n = 9 cells, 4 mice), with a strong bias towards inhibition (E / I Ratio = 0.36, CI = 0.17–0.73) (Fig. 8C–D). However, suppression of NDNF+ cells reduced VM-evoked IPSCs (fraction of control = 0.57 ± 0.05, p = 0.004) (Fig. 8C & Fig. S8), without impacting EPSCs (fraction of control = 1.02 ± 0.06, p = 0.91) (Fig. 8D & Fig. S8). These findings confirm that the VM-evoked inhibition of PT cells involves the activation of NDNF+ cells.

Lastly, to determine the functional impact of VM-evoked inhibition, we compared synaptic responses before and after bath application of GABA-R antagonists. Blocking inhibition significantly increased VM-evoked EPSPs (before drug = 118 ± 20 mV*ms, after drug = 275 ± 54 mV*ms, p = 0.0078; n= 8 cells, 7 mice) and dendritic Ca2+ signals (before drug = 2.5 ± 0.5 $\Delta G/G_{sat}$*ms, after drug = 4.6 ± 0.9 $\Delta G/G_{sat}$*ms, p = 0.016) (Fig. 8E–F). To approximate bursts of thalamic activity, we also examined the impact of inhibition on responses to stimulus trains of VM inputs (3 LED pulses @ 50 Hz). With intact inhibition, PT cells and PYRs displayed summating but subthreshold EPSPs (Fig. 8G); however, when inhibition was blocked, PT cells fired a barrage of APs (p-spike: before drug = 0.0 ± 0.0, after drug = 0.77 ± 0.15, p = 0.016) (Fig. 8G–H), with greatly increased dendritic Ca2+ signals (before drug = 5.0 ± 1.6 $\Delta G/G_{sat}$*ms, after drug = 28.5 ± 6.3 $\Delta G/G_{sat}$*ms, p = 0.0078) (Fig. 8G–H & Fig. S8). Importantly, these changes were not due to local network activity, as simultaneous recordings from PYRs remained subthreshold in all cases (Fig. 8G–H & Fig. S8). These results indicate that inhibition both prevents VM inputs from firing PT cells and suppresses dendritic Ca2+ signals. Together, our findings characterize a

monosynaptic input-output circuit between VM and PT cells, which is tightly regulated by strong thalamus-evoked inhibition mediated by NDNF+ cells in L1a.

DISCUSSION

Our findings demonstrate that two higher-order thalamic nuclei innervate distinct populations of L1 interneurons in the PFC. MD primarily drives VIP+ cells in L1b, which in turn inhibit L2/3 SOM+ cells, engaging a local disinhibitory circuit. In contrast, VM engages NDNF+ cells in L1a, which then inhibit L2/3 PV+ cells, along with L2/3 and L5 pyramidal cells. By targeting the apical dendrites of PT cells, NDNF+ cells robustly inhibit VM-mediated activation of dendritic Ca2+ signals. NDNF+ cells therefore participate in both a thalamus-evoked inhibitory circuit and a separate, distinct disinhibitory circuit. Together, these results indicate that higher-order thalamic inputs engage different inhibitory networks to have distinct functional influences on the PFC.

Thalamic nuclei are categorized in multiple ways, based on their cytology, inputs, and outputs (Jones, 1998; Kuramoto et al., 2017; Sherman and Guillery, 1996). In sensory cortex, first-order thalamus drives cells in L4 (Agmon and Connors, 1991; Cruikshank et al., 2010), whereas higher-order thalamus influences networks in other layers (Audette et al., 2018; Crandall et al., 2017; Williams and Holtmaat, 2019). In the PFC, thalamic inputs exclusively arrive from a variety of higher-order nuclei (Collins et al., 2018), with both MD and VM considered “secondary” based on their transcriptomic profiles (Phillips et al., 2019). However, these inputs have different axonal projections, with MD innervating L1b and L3, and VM arborizing in L1a. We previously found MD drives L2/3 pyramidal cells (Collins et al., 2018), and our new data indicate MD also activates L1b VIP+ cells. In contrast, VM engages NDNF+ cells in L1a, which in turn play a critical role in regulating the activity of L5 PT cells. These results highlight how synaptic connectivity provides an important additional metric for understanding the diversity of thalamic nuclei.

Recent whole-brain rabies tracing studies have not revealed major differences in thalamic innervation of interneurons in the PFC (Ährlund-Richter et al., 2019; Sun et al., 2019), which differs from our results. One explanation for this discrepancy is that we focused on L1 interneurons, motivated by dense thalamic axon to this layer. In contrast, rabies tracing pools inputs to cells across layers and cannot account for the strength and dynamics of presynaptic inputs or the intrinsic physiology of postsynaptic cells. Our data shows that the mechanisms behind differences in thalamic activation of L1 interneuron subtypes only emerge after voltage-clamp recordings to measure synaptic connections and current-clamp recordings to account for intrinsic membrane properties. For example, our rabies tracing data suggested both MD and VM connect with VIP+ and NDNF+ interneurons, and our voltage-clamp experiments show MD inputs are similar in strength at the two cells, but current-clamp recordings show MD preferentially activates VIP+ cells due to their higher intrinsic excitability. In contrast, VM inputs are much stronger at NDNF+ cells, which they selectively activate despite their lower intrinsic excitability. Together, our combined experimental approach demonstrates the importance of detailed circuit analysis considering the location of cells, postsynaptic physiology, and presynaptic dynamics.

Our results indicate that VM and MD engage two distinct classes of L1 interneurons in the PFC, which are segregated between L1a and L1b. Evidence from sensory cortices suggests that this sublaminar organization may be a general principle, with VIP+ cells consistently located further from the cortical surface (Abs et al., 2018; Schuman et al., 2019). Interestingly, MD targeting of VIP+ cells in PFC resembles activation of somatosensory VIP + cells by inputs from the motor cortex and higher-order thalamus (Lee et al., 2013; Williams and Holtmaat, 2019). VIP+ cells in turn inhibit SOM+ cells, a motif observed across cortex (Lee et al., 2013; Williams and Holtmaat, 2019), including the PFC (Pi et al., 2013). Thus, our results suggest that MD activates a conserved disinhibitory circuit, with the inhibition of SOM+ cells suppressing dendritic inhibition of pyramidal cells, potentially enabling dendritic electrogenesis and synaptic plasticity (Williams and Holtmaat, 2019). In contrast, VM strongly activates L1a NDNF+ cells, which in turn inhibit PV+ cells that synapse at the soma of pyramidal cells. A similar form of disinhibition via PV+ cells has been reported to drive a form of non-VIP+ dependent plasticity during auditory learning (Letzkus et al., 2011). Therefore, our results indicate that thalamic nuclei engage distinct inhibitory micro-circuits that can influence dendritic and somatic activity, with important implications for PFC function.

While cortical interneurons are often divided into cardinal groups, there is substantial heterogeneity in each of these populations (Markram et al., 2004; Tremblay et al., 2016). For example, SOM+ cells are amongst the most diverse neurons in the cortex (Tasic et al., 2018), with different subtypes mediating distinct functions (Hilscher et al., 2017; Naka et al., 2018; Tremblay et al., 2016; Xu et al., 2013) and the GIN line we used labels dendrite-targeting Martinotti cells (Oliva et al., 2000). Consistent with our findings, there is also a high probability of connection from VIP+ cells to SOM+ cells in superficial layers of visual cortex (Pfeffer et al., 2013), although targeting in deep layers may be more diverse (Zhou et al., 2017). Similarly, the G42 line used here only labels a subset of PV+ cells (Chattopadhyaya et al., 2004), although the functional diversity of the PV+ population is currently poorly understood. VIP+ cells also consist of different subtypes based on expression of calretinin (CR) and cholecystokinin (CCK) (Acsady et al., 1996; Tremblay et al., 2016), which have distinct morphology and physiology (Acsady et al., 1996; He et al., 2016). Many of the L1b VIP+ cells we recorded matched the VIP+ / CR+ subtype known to target other interneurons (Anastasiades et al., 2019), consistent with our output mapping of strong VIP+ → SOM+ connectivity. Lastly, NDNF+ cells comprise at least two subgroups, distinguished by expression of Neuropeptide Y (NPY), with late-spiking cells enriched in the NPY+ population (Schuman et al., 2019). In the future, it will be important to further refine our understanding of how these different interneuron subtypes respond to thalamic inputs and communicate with each other and pyramidal cells in superficial layers of the PFC.

In addition to synapsing on interneurons, NDNF+ cells also strongly contact both L2/3 and L5 pyramidal cells, with particularly strong connections onto L5 PT cells. Interestingly, this biased inhibition has recently been observed for PV+, SOM+ and CCK+ inputs onto L5 pyramidal cells (Anastasiades et al., 2018a; Liu et al., 2020). The axons of NDNF+ cells primarily arborize within L1, making most of their connections onto the distal apical dendrites of PT cells. Optogenetic activation of NDNF+ cells strongly inhibits PT cell apical

dendrites and suppresses the somatic ADP, as recently reported in sensory cortex (Abs et al., 2018). By measuring the spatial influence of this inhibition using 2-photon imaging, we further observed a complete block of local Ca2+ signals, which was highly restricted to the distal apical tuft. These findings complement our previous work on local $GABA_AR$-mediated dendritic inhibition, identifying NDNF+ cells as a subpopulation of 5HT3aR+ cells that strongly inhibit AP-evoked Ca2+ signals in unlabeled pyramidal cells (Marlin and Carter, 2014). SOM+ cells also inhibit dendritic Ca2+ signals in pyramidal cells (Chiu et al., 2013; Marlin and Carter, 2014), but are primarily activated by local connections (Kapfer et al., 2007). Interestingly, our results suggest that MD may relieve dendritic inhibition at pyramidal cells by activating VIP+ cells, suggesting contrasting roles for VM and MD in inhibitory control of dendritic electrogenesis.

In addition to activating interneurons, both MD and VM directly innervate the apical dendrites of PT cells, with weaker connections onto IT dendrites (Collins et al., 2018; Guo et al., 2018). This targeting appears specific to thalamic circuits, as it is not observed for callosal, hippocampal or amygdala inputs (Anastasiades et al., 2018a; Liu and Carter, 2018; Manoocheri & Carter, unpublished). Consistent with this connectivity, VM readily triggers dendritic Ca2+ signals, but only in PT cells and not IT cells, which reflects thalamic input rather than local network activity, because L2/3 pyramidal cells are quiescent. These dendritic Ca2+ signals are regulated by VM-evoked inhibition mediated by NDNF+ cells acting on GABA receptors. Although our ArchT experiments did not completely abolish VM-evoked IPSCs, the reduction is similar to related studies (Delevich et al., 2015; Lee et al., 2013). Incomplete suppression could be due to lateral inhibition between adjacent NDNF + cells (Fan et al., 2020) or variable ArchT expression. Blocking GABA receptors enhances dendritic Ca2+ signals and somatic EPSPs, allowing bursts of VM inputs to elicit action potentials. These dendritic non-linearities may play an important role in amplifying VM input to selectively recruit PT cells (Larkum and Zhu, 2002; Stuart et al., 1997).

Our results indicate that VM activation of PT cells is tightly controlled by NDNF+ cells, suggesting these L1 interneurons can gate long-range feed-back loops between thalamus and PFC. In principle, a variety of mechanisms could release this inhibition by regulating the activity of NDNF+ cells. First, depressing VM input or NDNF+ output, similar to feed-forward inhibition mediated via PV+ cells in sensory cortex (Cruikshank et al., 2010). Second, neuromodulation, including via selectively expressed acetylcholine or noradrenergic receptors (Brombas et al., 2014; Salgado et al., 2011). Third, local inhibition via SOM+ cells (Abs et al., 2018) or lateral inhibition via other NDNF+ cells (Fan et al., 2020). Fourth, long-range inputs from inhibitory regions, including the basal ganglia and basal forebrain (Saunders et al., 2015a, 2015b), which our rabies data show project to NDNF+ cells. In the future, it will be important to uncover which mechanisms are engaged, and how they contribute to VM-evoked firing and dendritic Ca2+ spikes in PT cells.

Our experiments suggest multiple ways in which MD and VM differentially impact specific microcircuits to shape activity in the PFC (Bolkan et al., 2017; Schmitt et al., 2017). MD input to L1b VIP+ cells may combine with input to L3 pyramidal cells (Collins et al., 2018) to maintain local excitation and support delay period activity (Bolkan et al., 2017; Schmitt et al., 2017). Similarly, MD input may also amplify cortical or BLA inputs to superficial layers

(Little and Carter, 2013; Schmitt et al., 2017), as suggested for higher-order thalamic inputs to sensory cortex (Williams and Holtmaat, 2019; Zhang and Bruno, 2019). Activation of superficial networks also influences deep layers, including connections onto L5 PT cells that "close the loop" between PFC and thalamus (Collins et al., 2018). By targeting their dendrites, VM can also directly and selectively engage PT cells, which innervate numerous downstream targets (Collins et al., 2018; Economo et al., 2018). Consistent with our findings, a recent study from sensory cortex showed how activity within PT dendrites plays an essential role in regulating cortical function via increasing outputs to thalamus and other regions (Takahashi et al., 2020). Therefore, VM-evoked activation of PT cell dendrites has important implications for cognitive behaviors that depend upon communication between PFC, thalamus and subcortical structures (Bolkan et al., 2017; Guo et al., 2017; Schmitt et al., 2017; Warden et al., 2012).

In summary, we have established that MD and VM have different influence on the PFC, depending on the presynaptic input, cortical sublayer, postsynaptic cell type, and subcellular compartment. Our findings add to a growing literature about how long-range inputs from the thalamus, cortex, amygdala, hippocampus and claustrum differentially engage PFC microcircuits (Anastasiades et al., 2018a; Cruikshank et al., 2012; Delevich et al., 2015; Jackson et al., 2018; Little and Carter, 2013; Liu and Carter, 2018; McGarry and Carter, 2016). Our observation that multiple thalamic nuclei engage L1 interneuron subtypes, which subsequently inhibit L2/3 interneurons, suggests an important role for thalamus in gating superficial layer pyramidal neurons. This includes a myriad of projection neurons, including cortico-cortical, cortico-amygdala and cortico-striatal neurons, in addition to PT cells. Therefore, our findings suggest thalamus plays a central role in orchestrating activity across PFC networks that engage many downstream targets, albeit through distinct mechanisms to studies of thalamo-cortical networks in sensory cortices (Audette et al., 2018; Crandall et al., 2017; Cruikshank et al., 2010). In the future, it will be important to study how other thalamic inputs influence the PFC, including from the intralaminar nuclei (Mandelbaum et al., 2019) and nucleus reuniens (Banks et al., 2020). Similarly, it will be important to test if the thalamic connectivity motifs observed in the PFC are present in other frontal cortices, including ALM (Guo et al., 2018). Our advancing understanding of these networks will help understand how they contribute to complex cognitive tasks associated with higher-order thalamo-cortical loops (Bolkan et al., 2017; Gao et al., 2018; Guo et al., 2017; Schmitt et al., 2017).

STAR METHODS

Resource Availability

Lead Contact: Further information and requests for resources and reagents should be directed to and will be fulfilled by the Lead Contact, Adam Carter (adam.carter@nyu.edu).

Materials Availability: This study did not generate new unique reagents.

Data and Code Availability: All data and codes generated during this study are available upon request.

Experimental Model and subject details

Acute slices were prepared from healthy, immune-competent P42-P90 wild-type mice, NDNF-Cre mice (Tasic et al., 2016), VIP-Cre mice (Taniguchi et al., 2011), 5HT3aR-Cre (Gong et al., 2003), VIP-Cre crossed to Ai14 reporter mice (Madisen et al., 2010), and NDNF-Cre or VIP-Cre crossed to G42 (Chattopadhyaya et al., 2004) or GIN (Oliva et al., 2000) interneuron reporter mice. Mice were bred on mixed background. No animals had been involved in previous procedures. Animals were group-housed with same-sex littermates in a dedicated animal care facility and were on a 12-h light/dark cycle at 18–23°C. Food and water were available *ad libitum*. All physiology and anatomy experiments used male and female mice, and no significant differences were found between groups. All procedures followed guidelines approved by the New York University animal welfare committee.

Method Details

No formal method for randomization was used and experimenters were not blind to experimental groups. No pre-test analyses were used to estimate sample sizes. No data were excluded from final analyses.

Stereotaxic injections.—P28-P50 mice were anesthetized with a mixture of ketamine and xylazine or isoflurane and head fixed in a stereotax (Kopf Instruments). A small craniotomy was made over the injection site, through which retrograde tracers and viruses were injected. Injection site coordinates were relative to bregma (mediolateral, dorsoventral, and rostrocaudal axes): PFC = ±0.3, −2.1, +2.2 mm (Allen mouse common coordinate framework (CCF): ±0.3, 2.35, 2.03 mm); anterior MD thalamus = −0.4, −3.5, −0.4 mm (Allen mouse CCF: −0.7, 1.2, −1.17 mm); anterior VM thalamus = −2.9, −3.4, −0.4 mm, at an angle of 30° from upright (Allen mouse CCF: −1.0, 0.15, −1.17 mm), PAG = −0.5, −3.0, −4.0 mm (Allen mouse CCF: −0.5, 2.01, −4.07 mm). For examples of thalamus injection sites, see Fig. S1 A–C. Borosilicate pipettes with 5–10 μm tip diameters were backfilled and 100–500 nl was pressure-injected using a Nanoject II (Drummond) with 30–45 second inter-injection intervals. For retrograde labeling, pipettes were filled with red retrobeads (Lumafluor) or cholera toxin subunit B (CTB) conjugated to Alexa 647 (Thermo Fisher). Axon labelling was achieved using AAV1-CB7-mCherry (UPenn Vector Core) or AAV1-hSyn-EGFP (UPenn Vector Core). Interneuron labelling was achieved using AAV1-CAG-FLEX-tdTomato (UPenn Vector Core) or AAV9-CAG-FLEX-EFGP (UPenn Vector Core). Optogenetic stimulation was achieved using AAV1-hSyn-hChR2-EYFP (UPenn Vector Core), AAV1-CAMKIIa-hChR2-mcherry (UPenn Vector Core), AAV1-EF1a-DIO-hChR2-EYFP (UPenn Vector Core), AAV1-EF1a-dflox-hChR2-mCherry (Addgene), or AAV expressing soma-tagged ChroME AAV9-CAG-DIO-ChronosM140E-ST-p2A-H2B-mRuby (Addgene) (Mardinly et al., 2018). Optogenetic inhibition was achieved using AAV9-FLEX-ArchT-GFP (UNC Vector Core). For ArchT experiments two separate injections were performed. AAV1-CAMKIIa-hChR2-mcherry was injected into VM then 14–20 days later AAV9-FLEX-ArchT-GFP was injected and allowed to express for an additional 8–10 days. This was necessary to avoid blue light mediated activation of ArchT, which was found to occur at longer expression durations. Following injections, the pipette was left in place for an additional 10 min before being slowly withdrawn. After all injections, animals were returned to their home cages for 1–4 weeks before being used for experiments.

Slice preparation.—Adult mice (P42-P90) were anesthetized with an intraperitoneal injection of a lethal dose of ketamine/xylazine and perfused intracardially with an ice-cold cutting solution containing (in mM): 65 sucrose, 76 NaCl, 25 $NaHCO_3$, 1.4 NaH_2PO_4, 25 glucose, 2.5 KCl, 7 $MgCl_2$, 0.4 Na-ascorbate, and 2 Na-pyruvate (bubbled with 95% O_2/5% CO_2). 300 μm coronal sections were cut in this solution and transferred to ACSF containing (in mM): 120 NaCl, 25 $NaHCO_3$, 1.4 NaH_2PO_4, 21 glucose, 2.5 KCl, 2 $CaCl_2$, 1 $MgCl_2$, 0.4 Na-ascorbate, and 2 Na-pyruvate (bubbled with 95% O_2/5% CO_2). Slices were recovered for 30 min at 35°C and stored for at least 30 min at 24°C. For thalamocortical optogenetics, the thalamus was also sectioned and inspected under a fluorescent dissection scope to confirm that ChR2 was targeted to MD or VM. If injections missed the target nucleus, slices were not recorded. In some cases, injection in VM led to ChR2 expression in adjacent nuclei such as VPL and VPM, but this was unlikely to influence our results, as labelling was often weak in these areas and our rabies tracing data suggest that input from these nuclei is at least an order of magnitude less than from VM (Table S2). With the exception of sCRACM and st-ChroME mapping experiments, which were performed at room temperature, recordings were conducted at 30–32°C.

Electrophysiology.—Targeted whole-cell recordings were made from projection neurons or interneurons in the prelimbic PFC using infrared-differential interference contrast. Layers were defined by distance from the pial surface, as described previously (Anastasiades et al., 2019). L1a and L1b were distinguished by subdividing the depth of L1 at its midpoint, with the inner half L1b and outer half L1a. IT and PT neurons were identified by the presence of retrobeads or CTB. Targeted recordings from L1 interneurons were performed using Cre-dependent fluorophore after injection with AAVs or crossing to Ai14 reporter mice.

For voltage-clamp experiments, borosilicate pipettes (3–5 MΩ) were filled with the following (in mM): 135 Cs-gluconate, 10 HEPES, 10 Na-phosphocreatine, 4 Mg_2-ATP, 0.4 NaGTP, 10 TEA, 2 QX-314, and 10 EGTA, pH 7.3 with CsOH (290–295 mOsm). For most current-clamp recordings, borosilicate pipettes (3–5 MΩ) were filled with the following (in mM): 135 K-gluconate, 7 KCl, 10 HEPES, 10 Na-phosphocreatine, 4 Mg_2-ATP, 0.4 NaGTP, and 0.5 EGTA, pH 7.3 with KOH (290–295 mOsm). For $GABA_B$ IPSP experiments borosilicate pipettes (3–5 MΩ) were filled with an internal solution with a low intracellular chloride solution (in mM): 130 K-gluconate, 1.5 $MgCl_2$, 10 HEPES, 10 Na-phosphocreatine, 2 Mg_2-ATP, 0.4 NaGTP, and 1.1 EGTA, pH 7.3 with KOH (290–295 mOsm). In some cases, 30 μM Alexa Fluor-594 or −488 (Thermo Fisher) were added to visualize morphology with two-photon microscopy, or 5% Biocytin for post-hoc recovery of morphology using streptavidin conjugated to Alexa 647 (Invitrogen). For Ca2+ imaging experiments, 0.5 mM Fluo-5F (Invitrogen) was added. In all voltage-clamp experiments, 10 μM CPP was used to block NMDA receptors. In some voltage-clamp experiments, 10 μM ZD-7288 was included to block HCN channels, 1 μM TTX was included to block action potentials (APs), along with 0.1 mM 4-AP and 4 mM external Ca2+ to restore presynaptic glutamate release. In some experiments, 10 μM NBQX was used to block AMPA receptors, and 10 μM gabazine plus 2 μM CGP was used to block $GABA_A$ and $GABA_B$ receptors. All chemicals were from Sigma or Tocris Bioscience. IPSCs were recorded at +10 mV and EPSCs were recorded at

−60 mV unless otherwise stated. Current-clamp recordings were performed at the resting membrane potential, or at −50 mV for $GABA_B$ IPSP pharmacology experiments.

Physiology data were collected with a Multiclamp 700B amplifier (Axon Instruments) and National Instruments boards using custom software in MATLAB (MathWorks). Signals were sampled at 10 kHz and filtered at either 5 kHz for current-clamp recordings or 2 kHz for voltage-clamp recordings. Series resistance was 10–25 MΩ and not compensated.

Optogenetics.—Glutamate release was triggered by activating channelrhodopsin-2 (ChR2) present in presynaptic terminals of either thalamic inputs to the PFC, or local circuit interneurons as previously described (Anastasiades et al., 2018a; Little and Carter, 2012). ChR2 was activated with 1–8 ms pulses of 473 nm light from a blue light-emitting diode (LED; 473 nm; Thorlabs) through a 10X 0.3 NA objective (Olympus) with a power range of 0.1–20 mW. For widefield recordings in the PFC, the objective was always centered 200 μm from the pial surface of the cortex. For focused optogenetic stimulation over the apical or basal dendrites blue (473 nm) LED light was focused through a 60X 1.0NA objective (Olympus). For ArchT mediated suppression of activity this was interleaved with light from a yellow (590 nm) light focused through the same 60X 1.0NA objective. Subcellular targeting (sCRACM) experiments were performed using a Polygon DMD device (Mightex) focused through a 10X 0.3 NA objective (Olympus) with a 75 μm pixel size. Pulses were delivered at 1 Hz using a pseudo-random 10 × 10 grid pattern, yielding an effective mapping area of 750 μm × 750 μm. Experiments used a 4 ms LED pulse yielding an effective power of 0.17 mW per pixel.

Soma-restricted optogenetics.—To map the outputs of st-ChroME+ interneurons, stimulation parameters were developed to produce robust, spatially restricted AP firing of these cells. Expression time was tightly controlled (14–16 days post injection) to ensure reliable, yet spatially restricted, firing across the presynaptic population. Calibration recordings were performed in cell-attached mode to avoid perturbing the intracellular environment of the cell. A blue (473 nm) LED was passed through a Polygon DMD device (Mightex) and focused through a 10X 0.3 NA objective (Olympus) with pixel size calibrated to 75 μm. Pulses were delivered at 1 Hz using a pseudo-random 10 × 10 grid pattern, yielding an effective mapping area of 750 μm × 750 μm. Experiments used a 1 ms LED pulse yielding an effective power of 0.02 mW per pixel. Presynaptic APs occurred within 30 ms of LED onset and a postsynaptic IPSCs detection window was set to include responses 100 ms after LED onset to calculate the IPSC peak amplitude per pixel, as described previously (Anastasiades et al., 2018b).

Two-photon microscopy.—Two-photon imaging was performed on a custom microscope, as previously described (Chalifoux and Carter, 2010; Marlin and Carter, 2014). Briefly, a Titanium:Sapphire laser (Coherent Ultra II) tuned to 810 nm was used to excite Alexa Fluor-594 or −488 and Fluo-5F to image dendrite morphology and monitor Ca2+ signals, respectively. Line scans were acquired across dendrites or dendrite-spine pairs at 500 Hz. Reference frame scans were routinely taken to correct for any spatial drifts over time at the imaging location. Ca2+ signals were quantified as the change in Fluo-5F fluorescence [green (G)] normalized to the Alexa Fluor 594 fluorescence [red (R)], giving

units of ΔG/R. These signals were then normalized to the G_{sat}/R value measured with a saturating concentration of Ca2+ added to the internal solution in a thin-walled pipette, giving final measurements in units of $\Delta G/G_{sat}$. Recordings were discarded if an increase in baseline fluorescence was detected, which could indicate photo damage. Experiments testing the impact of optogenetic activation of NDNF+ interneurons on AP Ca2+ signals involved four interleaved trials: 1 = no APs + no LED, 2 = 3 × APs + no LED, 3 = no APs + LED, 4 = 3 × APs + LED. ChR2 activation (2ms light pulse) was followed after 10ms by 3 × 1ms, 1.5–3 nA somatic current steps delivered at 100 Hz to drive AP generation (Marlin and Carter, 2014). For experiments testing the dendritic Ca2+ response to VM axon stimulation, NBQX, CCP, GZ and CGP were added to the bath at the end of the experiment, and line scans were repeated to test for LED artifacts. All Imaging was performed with a 60X 1.0NA objective (Olympus). A fast shutter was closed for 25ms after light delivery to protect the PMTs during any experiments involving imaging during LED stimulation. Morphological reconstruction and analysis of 2-photon image stacks were by manually tracing over max projections of the reconstructed neurons.

Rabies virus tracing.—For monosynaptic rabies virus tracing, AAV1-EF1a-FLEX-TVA-Cherry (130 nL) (UNC Vector Core) and AAV9-CAG-FLEX-oG (450 nL) (Salk) were injected into a single hemisphere of the PFC of either NDNF-Cre or VIP-Cre mice. After allowing 4–5 weeks for expression of these helper viruses, 750 nL of SADΔG-GFP(EnvA) rabies virus (Salk) was injected at the same location. After an additional 8 days to allow for monosynaptic retrograde labeling, mice were perfused, and slices prepared for fluorescent microscopy.

Histology.—Mice were anesthetized and perfused intracardially with 0.01 M PBS followed by 4% PFA. Brains were stored in 4% PFA for 12–18 hours at 4°C before being washed three times in 0.01 M PBS. Slices were cut on a VT-1000S vibratome (Leica) at 75 μm thickness and placed on gel-coated glass slides. ProLong Gold anti-fade reagent with DAPI (Invitrogen) or VectaShield with DAPI (Vector Labs) was applied to the surface of the slices, which were then covered with a glass coverslip. Fluorescent images were taken on an Olympus VS120 microscope, using a 10X 0.25NA objective (Olympus) or on a Leica TCS SP8 confocal microscope, using either a 10X 0.4NA or 20X 0.75NA objective (Olympus).

Data analysis.—Off-line analysis was performed using Igor Pro (WaveMetrics). For current-clamp recordings, input resistance was measured using the steady-state response to a 500 ms, −10, −20 or −50 pA current injection. The membrane time constant (tau) was measured using exponential fits to these hyperpolarizations. Action potential latencies were measured as the time between onset of current injection and membrane voltage crossing 0 mV for spikes at rheobase. The ADP was calculated as the area under the curve of the voltage trace in the 25 ms following termination of the third AP in a burst of 3 APs delivered at 100 Hz. For voltage-clamp recordings, EPSC and IPSC amplitudes were measured as the average value across 1 ms around the peak response.

Cell counting was performed in ImageJ using the Cell Counter plugin. For cumulative frequency plots of L1 interneurons the depth of each cell was determined and normalized to the depth of L1, with the L1/2 border determined for each slice based on DAPI labeling.

Axon distributions in PFC and thalamus were quantified using un-binned fluorescence. The average fluorescence profile for each slice was peak-normalized and multiple individual traces are shown. For rabies tracing labeled cell bodies were manually counted for every slice between rostro-caudal coordinates +2.2 to −5.0 relative to bregma. Presynaptic input regions were determined relative to the Allen Brain Atlas at the appropriate rostro-caudal co-ordinate. For cross laminar analysis of rabies labeled cells in the local circuit, the distance from the pial surface was used to sort cells into 25 μm bins for those cells assigned to the prelimbic subdivision of the mPFC. The number of cells per bin was averaged across 3 slices from each animal.

Quantification and Statistical Analysis

N values are reported within the Results and Supplemental Figure legends as number of recorded cells (for physiology) or number of animals (for anatomy). Summary data are reported in the text and figures as arithmetic mean ± SEM unless otherwise stated. Ratio data are displayed in figures on logarithmic axes and reported as geometric mean ± 95% confidence interval (CI). In some graphs with three or more traces, SEM waves are omitted for clarity. Statistical analyses were performed using Prism 7.0 (GraphPad Software). Hierarchical cluster analysis was performed in MATLAB (MathWorks). Comparisons between unpaired data were performed using two-tailed Mann-Whitney tests. Comparisons between data recorded in pairs were performed using two-tailed Wilcoxon matched-pairs signed rank tests. Ratio data were compared to a theoretical median of 1 using Wilcoxon signed rank tests. For rabies tracing, comparisons were performed using an unpaired t-test correcting for multiple comparisons using the Holm-Sidak method. Significance was defined as $p < 0.05$.

Supplementary Material

Refer to Web version on PubMed Central for supplementary material.

ACKNOWLEDGEMENTS

We thank the Carter lab for helpful discussions and comments on the manuscript. This work was supported by NIH T32 GM007308 (DPC), NIH F30 MH117859 (DPC) and NIH R01 MH085974 (AGC).

REFERENCES

Abs E, Poorthuis RB, Apelblat D, Muhammad K, Pardi MB, Enke L, Kushinsky D, Pu D-L, Eizinger MF, Conzelmann K-K, et al. (2018). Learning-Related Plasticity in Dendrite-Targeting Layer 1 Interneurons. Neuron 100, 684–699. [PubMed: 30269988]

Acsady L, Gorcs TJ, and Freund TF (1996). Different populations of vasoactive intestinal polypeptide-immunoreactive interneurons are specialized to control pyramidal cells or interneurons in the hippocampus. Neuroscience 73, 317–334. [PubMed: 8783252]

Agmon A, and Connors BW (1991). Thalamocortical responses of mouse somatosensory (barrel) cortex in vitro. Neuroscience 41, 365–379. [PubMed: 1870696]

Ährlund-Richter S, Xuan Y, Lunteren van JA, Kim H, Ortiz C, Dorocic IP, Meletis K, and Carlén M (2019). A whole-brain atlas of monosynaptic input targeting four different cell types in the medial prefrontal cortex of the mouse. Nat. Neurosci 22, 657–668. [PubMed: 30886408]

Anastasiades PG, Marlin JJ, and Carter AG (2018a). Cell-Type Specificity of Callosally Evoked Excitation and Feedforward Inhibition in the Prefrontal Cortex. Cell Rep. 22, 679–692. [PubMed: 29346766]

Anastasiades PG, Marques-Smith A, and Butt SJB (2018b). Studies of cortical connectivity using optical circuit mapping methods. J. Physiol 596, 145–162. [PubMed: 29110301]

Anastasiades PG, Boada C, and Carter AG (2019). Cell-Type-Specific D1 Dopamine Receptor Modulation of Projection Neurons and Interneurons in the Prefrontal Cortex. Cereb. Cortex 29, 3224–3242. [PubMed: 30566584]

Audette NJ, Urban-Ciecko J, Matsushita M, and Barth AL (2018). POm Thalamocortical Input Drives Layer-Specific Microcircuits in Somatosensory Cortex. Cereb. Cortex 28, 1312–1328. [PubMed: 28334225]

Baker CA, Elyada YM, Parra A, and Bolton MM (2016). Cellular resolution circuit mapping with temporal-focused excitation of soma-targeted channelrhodopsin. Elife 5, e14193. [PubMed: 27525487]

Banks PJ, Warburton EC, and Bashir ZI (2020). Plasticity in prefrontal cortex induced by coordinated nucleus reuniens and hippocampal synaptic transmission. BioRxiv 2020.07.11.197798.

Bolkan SS, Stujenske JM, Parnaudeau S, Spellman TJ, Rauffenbart C, Abbas AI, Harris AZ, Gordon JA, and Kellendonk C (2017). Thalamic projections sustain prefrontal activity during working memory maintenance. Nat. Neurosci 20, 987–996. [PubMed: 28481349]

Brombas A, Fletcher LN, and Williams SR (2014). Activity-Dependent Modulation of Layer 1 Inhibitory Neocortical Circuits by Acetylcholine. J. Neurosci 34, 1932–1941. [PubMed: 24478372]

Chalifoux JR, and Carter AG (2010). GABAB Receptors Modulate NMDA Receptor Calcium Signals in Dendritic Spines. Neuron 66, 101–113. [PubMed: 20399732]

Chalifoux JR, and Carter AG (2011). GABAB Receptor Modulation of Voltage-Sensitive Calcium Channels in Spines and Dendrites. J. Neurosci 31, 4221–4232. [PubMed: 21411663]

Chattopadhyaya B, Cristo GD, Higashiyama H, Knott GW, Kuhlman SJ, Welker E, and Huang ZJ (2004). Experience and Activity-Dependent Maturation of Perisomatic GABAergic Innervation in Primary Visual Cortex during a Postnatal Critical Period. J. Neurosci 24, 9598–9611. [PubMed: 15509747]

Chiu CQ, Lur G, Morse TM, Carnevale NT, Ellis-Davies G, and Higley MJ (2013). Compartmentalization of GABAergic Inhibition by Dendritic Spines. Science 340, 759–762. [PubMed: 23661763]

Chow BY, Han X, Dobry AS, Qian X, Chuong AS, Li M, Henninger MA, Belfort GM, Lin Y, Monahan PE, et al. (2010). High-performance genetically targetable optical neural silencing by light-driven proton pumps. Nature 463, 98–102. [PubMed: 20054397]

Chu Z, Galarreta M, and Hestrin S (2003). Synaptic Interactions of Late-Spiking Neocortical Neurons in Layer 1. J. Neurosci 23, 96–102. [PubMed: 12514205]

Collins DP, Anastasiades PG, Marlin JJ, and Carter AG (2018). Reciprocal Circuits Linking the Prefrontal Cortex with Dorsal and Ventral Thalamic Nuclei. Neuron 98, 366–379. [PubMed: 29628187]

Crandall SR, Patrick SL, Cruikshank SJ, and Connors BW (2017). Infrabarrels Are Layer 6 Circuit Modules in the Barrel Cortex that Link Long-Range Inputs and Outputs. Cell Rep. 21, 3065–3078. [PubMed: 29241536]

Cruikshank SJ, Urabe H, Nurmikko AV, and Connors BW (2010). Pathway-Specific Feedforward Circuits between Thalamus and Neocortex Revealed by Selective Optical Stimulation of Axons. Neuron 65, 230–245. [PubMed: 20152129]

Cruikshank SJ, Ahmed OJ, Stevens TR, Patrick SL, Gonzalez AN, Elmaleh M, and Connors BW (2012). Thalamic Control of Layer 1 Circuits in Prefrontal Cortex. J. Neurosci 32, 17813–17823. [PubMed: 23223300]

Delevich K, Tucciarone J, Huang ZJ, and Li B (2015). The Mediodorsal Thalamus Drives Feedforward Inhibition in the Anterior Cingulate Cortex via Parvalbumin Interneurons. J. Neurosci 35, 5743–5753. [PubMed: 25855185]

Economo MN, Viswanathan S, Tasic B, Bas E, Winnubst J, Menon V, Graybuck LT, Nguyen TN, Smith KA, Yao Z, et al. (2018). Distinct descending motor cortex pathways and their roles in movement. Nature 563, 79–84. [PubMed: 30382200]

Fan LZ, Kheifets S, Böhm UL, Wu H, Piatkevich KD, Xie ME, Parot V, Ha Y, Evans KE, Boyden ES, et al. (2020). All-Optical Electrophysiology Reveals the Role of Lateral Inhibition in Sensory Processing in Cortical Layer 1. Cell 180, 521–535. [PubMed: 31978320]

Gabbott PLA, Warner TA, Jays PRL, Salway P, and Busby SJ (2005). Prefrontal cortex in the rat: Projections to subcortical autonomic, motor, and limbic centers. J. Comp. Neurol 492, 145–177. [PubMed: 16196030]

Gao Z, Davis C, Thomas AM, Economo MN, Abrego AM, Svoboda K, Zeeuw CID, and Li N (2018). A cortico-cerebellar loop for motor planning. Nature 563, 113–116. [PubMed: 30333626]

Gong S, Zheng C, Doughty ML, Losos K, Didkovsky N, Schambra UB, Nowak NJ, Joyner A, Leblanc G, Hatten ME, et al. (2003). A gene expression atlas of the central nervous system based on bacterial artificial chromosomes. Nature 425, 917–925. [PubMed: 14586460]

Guo K, Yamawaki N, Svoboda K, and Shepherd GMG (2018). Anterolateral Motor Cortex Connects with a Medial Subdivision of Ventromedial Thalamus through Cell Type-Specific Circuits, Forming an Excitatory Thalamo-Cortico-Thalamic Loop via Layer 1 Apical Tuft Dendrites of Layer 5B Pyramidal Tract Type Neurons. J. Neurosci 38, 8787–8797. [PubMed: 30143573]

Guo ZV, Inagaki HK, Daie K, Druckmann S, Gerfen CR, and Svoboda K (2017). Maintenance of persistent activity in a frontal thalamocortical loop. Nature 545, 181–186. [PubMed: 28467817]

Han X, Chow BY, Zhou H, Klapoetke NC, Chuong A, Rajimehr R, Yang A, Baratta MV, Winkle J, Desimone R, et al. (2011). A High-Light Sensitivity Optical Neural Silencer: Development and Application to Optogenetic Control of Non-Human Primate Cortex. Front. Syst. Neurosci 5, 18. [PubMed: 21811444]

Harris KD, and Shepherd GMG (2015). The neocortical circuit: themes and variations. Nat. Neurosci 18, 170–181. [PubMed: 25622573]

He M, Tucciarone J, Lee S, Nigro MJ, Kim Y, Levine JM, Kelly SM, Krugikov I, Wu P, Chen Y, et al. (2016). Strategies and Tools for Combinatorial Targeting of GABAergic Neurons in Mouse Cerebral Cortex. Neuron 91, 1228–1243. [PubMed: 27618674]

Hilscher MM, Leão RN, Edwards SJ, Leão KE, and Kullander K (2017). Chrna2-Martinotti Cells Synchronize Layer 5 Type A Pyramidal Cells via Rebound Excitation. PLOS Biol. 15, e2001392. [PubMed: 28182735]

Honjoh S, Sasai S, Schiereck SS, Nagai H, Tononi G, and Cirelli C (2018). Regulation of cortical activity and arousal by the matrix cells of the ventromedial thalamic nucleus. Nat. Commun 9, 2100. [PubMed: 29844415]

Huang AS, Rogers BP, and Woodward ND (2019). Disrupted modulation of thalamus activation and thalamocortical connectivity during dual task performance in schizophrenia. Schizophr. Res 210, 270–277. [PubMed: 30630706]

Jackson J, Karnani MM, Zemelman BV, Burdakov D, and Lee AK (2018). Inhibitory Control of Prefrontal Cortex by the Claustrum. Neuron 99, 1029–1039. [PubMed: 30122374]

Jiang X, Wang G, Lee AJ, Stornetta RL, and Zhu JJ (2013). The organization of two new cortical interneuronal circuits. Nat. Neurosci 16, 210–218. [PubMed: 23313910]

Jones EG (1998). Viewpoint: the core and matrix of thalamic organization. Neuroscience 85, 331–345. [PubMed: 9622234]

Kapfer C, Glickfeld LL, Atallah BV, and Scanziani M (2007). Supralinear increase of recurrent inhibition during sparse activity in the somatosensory cortex. Nat. Neurosci 10, 743–753. [PubMed: 17515899]

Kuramoto E, Pan S, Furuta T, Tanaka YR, Iwai H, Yamanaka A, Ohno S, Kaneko T, Goto T, and Hioki H (2017). Individual mediodorsal thalamic neurons project to multiple areas of the rat prefrontal cortex: A single neuron-tracing study using virus vectors. J. Comp. Neurol 525, 166–185. [PubMed: 27275581]

Larkum ME, and Zhu JJ (2002). Signaling of Layer 1 and Whisker-Evoked Ca2+ and Na+ Action Potentials in Distal and Terminal Dendrites of Rat Neocortical Pyramidal Neurons In Vitro and In Vivo. J. Neurosci 22, 6991–7005. [PubMed: 12177197]

Larkum ME, Kaiser KMM, and Sakmann B (1999). Calcium electrogenesis in distal apical dendrites of layer 5 pyramidal cells at a critical frequency of back-propagating action potentials. Proc. Natl. Acad. Sci 96, 14600–14604. [PubMed: 10588751]

Lee S, Kruglikov I, Huang ZJ, Fishell G, and Rudy B (2013). A disinhibitory circuit mediates motor integration in the somatosensory cortex. Nat. Neurosci 16, 1662–1670. [PubMed: 24097044]

Letzkus JJ, Wolff SBE, Meyer EMM, Tovote P, Courtin J, Herry C, and Lüthi A (2011). A disinhibitory microcircuit for associative fear learning in the auditory cortex. Nature 480, 331–335. [PubMed: 22158104]

Little JP, and Carter AG (2012). Subcellular synaptic connectivity of layer 2 pyramidal neurons in the medial prefrontal cortex. J Neurosci 32, 12808–12819. [PubMed: 22973004]

Little JP, and Carter AG (2013). Synaptic Mechanisms Underlying Strong Reciprocal Connectivity between the Medial Prefrontal Cortex and Basolateral Amygdala. J. Neurosci 33, 15333–15342. [PubMed: 24068800]

Liu X, and Carter AG (2018). Ventral Hippocampal Inputs Preferentially Drive Corticocortical Neurons in the Infralimbic Prefrontal Cortex. J Neurosci 38, 7351–7363. [PubMed: 29959235]

Liu X, Dimidschstein J, Fishell G, and Carter AG (2020). Hippocampal inputs engage CCK+ interneurons to mediate endocannabinoid-modulated feed-forward inhibition in the prefrontal cortex. BioRxiv 2020.03.12.988881.

Madisen L, Zwingman TA, Sunkin SM, Oh SW, Zariwala HA, Gu H, Ng LL, Palmiter RD, Hawrylycz MJ, Jones AR, et al. (2010). A robust and high-throughput Cre reporting and characterization system for the whole mouse brain. Nat. Neurosci 13, 133–140. [PubMed: 20023653]

Mandelbaum G, Taranda J, Haynes TM, Hochbaum DR, Huang KW, Hyun M, Venkataraju KU, Straub C, Wang W, Robertson K, et al. (2019). Distinct Cortical-Thalamic-Striatal Circuits through the Parafascicular Nucleus. Neuron 102, 636–652. [PubMed: 30905392]

Mardinly AR, Oldenburg IA, Pégard NC, Sridharan S, Lyall EH, Chesnov K, Brohawn SG, Waller L, and Adesnik H (2018). Precise multimodal optical control of neural ensemble activity. Nat. Neurosci 21, 881–893. [PubMed: 29713079]

Markram H, Toledo-Rodriguez M, Wang Y, Gupta A, Silberberg G, and Wu C (2004). Interneurons of the neocortical inhibitory system. Nat. Rev. Neurosci 5, 793–807. [PubMed: 15378039]

Marlin JJ, and Carter AG (2014). GABA-A Receptor Inhibition of Local Calcium Signaling in Spines and Dendrites. J. Neurosci 34, 15898–15911. [PubMed: 25429132]

McGarry LM, and Carter AG (2016). Inhibitory Gating of Basolateral Amygdala Inputs to the Prefrontal Cortex. J. Neurosci 36, 9391–9406. [PubMed: 27605614]

Naka A, Veit J, Shababo B, Chance RK, Risso D, Stafford D, Snyder B, Egladyous A, Chu D, Sridharan S, et al. (2018). Complementary networks of cortical somatostatin interneurons enforce layer specific control. eLife 8, e43696.

Oláh S, Komlósi G, Szabadics J, Varga C, Tóth É, Barzó P, and Tamás G (2007). Output of Neurogliaform Cells to Various Neuron Types in the Human and Rat Cerebral Cortex. Front. Neural Circuits 1 ,4. [PubMed: 18946546]

Oláh S, Füle M, Komlósi G, Varga C, Báldi R, Barzó P, and Tamás G (2009). Regulation of cortical microcircuits by unitary GABA-mediated volume transmission. Nature 461, 1278–1281. [PubMed: 19865171]

Oliva AA, Jiang M, Lam T, Smith KL, and Swann JW (2000). Novel Hippocampal Interneuronal Subtypes Identified Using Transgenic Mice That Express Green Fluorescent Protein in GABAergic Interneurons. J. Neurosci 20, 3354–3368. [PubMed: 10777798]

Ouhaz Z, Fleming H, and Mitchell AS (2018). Cognitive Functions and Neurodevelopmental Disorders Involving the Prefrontal Cortex and Mediodorsal Thalamus. Front. Neurosci 12, 33. [PubMed: 29467603]

Palmer LM, Schulz JM, Murphy SC, Ledergerber D, Murayama M, and Larkum ME (2012). The Cellular Basis of GABAB-Mediated Interhemispheric Inhibition. Science 335, 989–993. [PubMed: 22363012]

Pérez-Garci E, Gassmann M, Bettler B, and Larkum ME (2006). The GABAB1b Isoform Mediates Long-Lasting Inhibition of Dendritic Ca2+ Spikes in Layer 5 Somatosensory Pyramidal Neurons. Neuron 50, 603–616. [PubMed: 16701210]

Pergola G, Danet L, Pitel A-L, Carlesimo GA, Segobin S, Pariente J, Suchan B, Mitchell AS, and Barbeau EJ (2018). The Regulatory Role of the Human Mediodorsal Thalamus. Trends Cogn. Sci 22, 1011–1025. [PubMed: 30236489]

Petreanu L, Mao T, Sternson SM, and Svoboda K (2009). The subcellular organization of neocortical excitatory connections. Nature 457, 1142–1145. [PubMed: 19151697]

Pfeffer CK, Xue M, He M, Huang ZJ, and Scanziani M (2013). Inhibition of inhibition in visual cortex: the logic of connections between molecularly distinct interneurons. Nat. Neurosci 16, 1068–1076. [PubMed: 23817549]

Phillips JW, Schulmann A, Hara E, Winnubst J, Liu C, Valakh V, Wang L, Shields BC, Korff W, Chandrashekar J, et al. (2019). A repeated molecular architecture across thalamic pathways. Nat. Neurosci 1925–1935. [PubMed: 31527803]

Pi H-J, Hangya B, Kvitsiani D, Sanders JI, Huang ZJ, and Kepecs A (2013). Cortical interneurons that specialize in disinhibitory control. Nature 503, 521–524. [PubMed: 24097352]

Rubio-Garrido P, Pérez-de-Manzo F, Porrero C, Galazo MJ, and Clascá F (2009). Thalamic Input to Distal Apical Dendrites in Neocortical Layer 1 Is Massive and Highly Convergent. Cereb. Cortex 19, 2380–2395. [PubMed: 19188274]

Salgado H, Garcia-Oscos F, Patel A, Martinolich L, Nichols JA, Dinh L, Roychowdhury S, Tseng K-Y, and Atzori M (2011). Layer-Specific Noradrenergic Modulation of Inhibition in Cortical Layer II/III. Cereb. Cortex N. Y. NY 21, 212–221.

Saunders A, Oldenburg IA, Berezovskii VK, Johnson CA, Kingery ND, Elliott HL, Xie T, Gerfen CR, and Sabatini BL (2015a). A direct GABAergic output from the basal ganglia to frontal cortex. Nature 521, 85–89. [PubMed: 25739505]

Saunders A, Granger AJ, and Sabatini BL (2015b). Corelease of acetylcholine and GABA from cholinergic forebrain neurons. Elife 4, e06412.

Schmitt LI, Wimmer RD, Nakajima M, Happ M, Mofakham S, and Halassa MM (2017). Thalamic amplification of cortical connectivity sustains attentional control. Nature 545, 219–223. [PubMed: 28467827]

Schuman B, Machold RP, Hashikawa Y, Fuzik J, Fishell GJ, and Rudy B (2019). Four Unique Interneuron Populations Reside in Neocortical Layer 1. J. Neurosci 39, 125–139. [PubMed: 30413647]

Sherman SM, and Guillery RW (1996). Functional organization of thalamocortical relays. J. Neurophysiol 76, 1367–1395. [PubMed: 8890259]

Stuart GJ, and Sakmann B (1994). Active propagation of somatic action potentials into neocortical pyramidal cell dendrites. Nature 367, 69–72. [PubMed: 8107777]

Stuart G, Schiller J, and Sakmann B (1997). Action potential initiation and propagation in rat neocortical pyramidal neurons. J. Physiol 505, 617–632. [PubMed: 9457640]

Sun Q, Li X, Ren M, Zhao M, Zhong Q, Ren Y, Luo P, Ni H, Zhang X, Zhang C, et al. (2019). A whole-brain map of long-range inputs to GABAergic interneurons in the mouse medial prefrontal cortex. Nat. Neurosci 22, 1357–1370. [PubMed: 31285615]

Takahashi N, Ebner C, Sigl-Glöckner J, Moberg S, Nierwetberg S, and Larkum ME (2020). Active dendritic currents gate descending cortical outputs in perception. Nat. Neurosci 1–9. [PubMed: 31844312]

Taniguchi H, He M, Wu P, Kim S, Paik R, Sugino K, Kvitsani D, Fu Y, Lu J, Lin Y, et al. (2011). A Resource of Cre Driver Lines for Genetic Targeting of GABAergic Neurons in Cerebral Cortex. Neuron 71, 995–1013. [PubMed: 21943598]

Tasic B, Menon V, Nguyen TN, Kim TK, Jarsky T, Yao Z, Levi B, Gray LT, Sorensen SA, Dolbeare T, et al. (2016). Adult Mouse Cortical Cell Taxonomy by Single Cell Transcriptomics. Nat. Neurosci 19, 335–346. [PubMed: 26727548]

Tasic B, Yao Z, Graybuck LT, Smith KA, Nguyen TN, Bertagnolli D, Goldy J, Garren E, Economo MN, Viswanathan S, et al. (2018). Shared and distinct transcriptomic cell types across neocortical areas. Nature 563, 72–78. [PubMed: 30382198]

Tremblay R, Lee S, and Rudy B (2016). GABAergic Interneurons in the Neocortex: From Cellular Properties to Circuits. Neuron 91, 260–292. [PubMed: 27477017]

Wall NR, Wickersham IR, Cetin A, Parra MDL, and Callaway EM (2010). Monosynaptic circuit tracing in vivo through Cre-dependent targeting and complementation of modified rabies virus. Proc. Natl. Acad. Sci 107, 21848–21853. [PubMed: 21115815]

Warden MR, Selimbeyoglu A, Mirzabekov JJ, Lo M, Thompson KR, Kim S-Y, Adhikari A, Tye KM, Frank LM, and Deisseroth K (2012). A prefrontal cortex–brainstem neuronal projection that controls response to behavioural challenge. Nature 492, 428–432. [PubMed: 23160494]

Williams LE, and Holtmaat A (2019). Higher-Order Thalamocortical Inputs Gate Synaptic Long-Term Potentiation via Disinhibition. Neuron 101, 91–102. [PubMed: 30472077]

Wozny C, and Williams SR (2011). Specificity of Synaptic Connectivity between Layer 1 Inhibitory Interneurons and Layer 2/3 Pyramidal Neurons in the Rat Neocortex. Cereb. Cortex N. Y. NY 21, 1818–1826.

Xu H, Jeong HY, Tremblay R, and Rudy B (2013). Neocortical somatostatin-expressing GABAergic interneurons disinhibit the thalamorecipient layer 4. Neuron 77, 155–167. [PubMed: 23312523]

Zhang W, and Bruno RM (2019). High-order thalamic inputs to primary somatosensory cortex are stronger and longer lasting than cortical inputs. ELife 8, e44158. [PubMed: 30741160]

Zhou F-M, and Hablitz JJ (1996). Morphological properties of intracellularly labeled layer I neurons in rat neocortex. J. Comp. Neurol 376, 198–213. [PubMed: 8951637]

Zhou X, Rickmann M, Hafner G, and Staiger JF (2017). Subcellular Targeting of VIP Boutons in Mouse Barrel Cortex is Layer-Dependent and not Restricted to Interneurons. Cereb. Cortex N. Y. NY 27, 5353–5368.

Zhu JJ, and Connors BW (1999). Intrinsic Firing Patterns and Whisker-Evoked Synaptic Responses of Neurons in the Rat Barrel Cortex. J. Neurophysiol 81, 1171–1183. [PubMed: 10085344]

Highlights

- Prefrontal cortex L1 has sublayers distinguished by thalamic axons from VM and MD
- VM and MD drive parallel L1 microcircuits comprised of NDNF and VIP interneurons
- NDNF and VM synapses are highly enriched at the apical dendrites of L5 PT cells
- NDNF-mediated dendritic inhibition controls VM-evoked Ca2+ signals at L5 PT cells

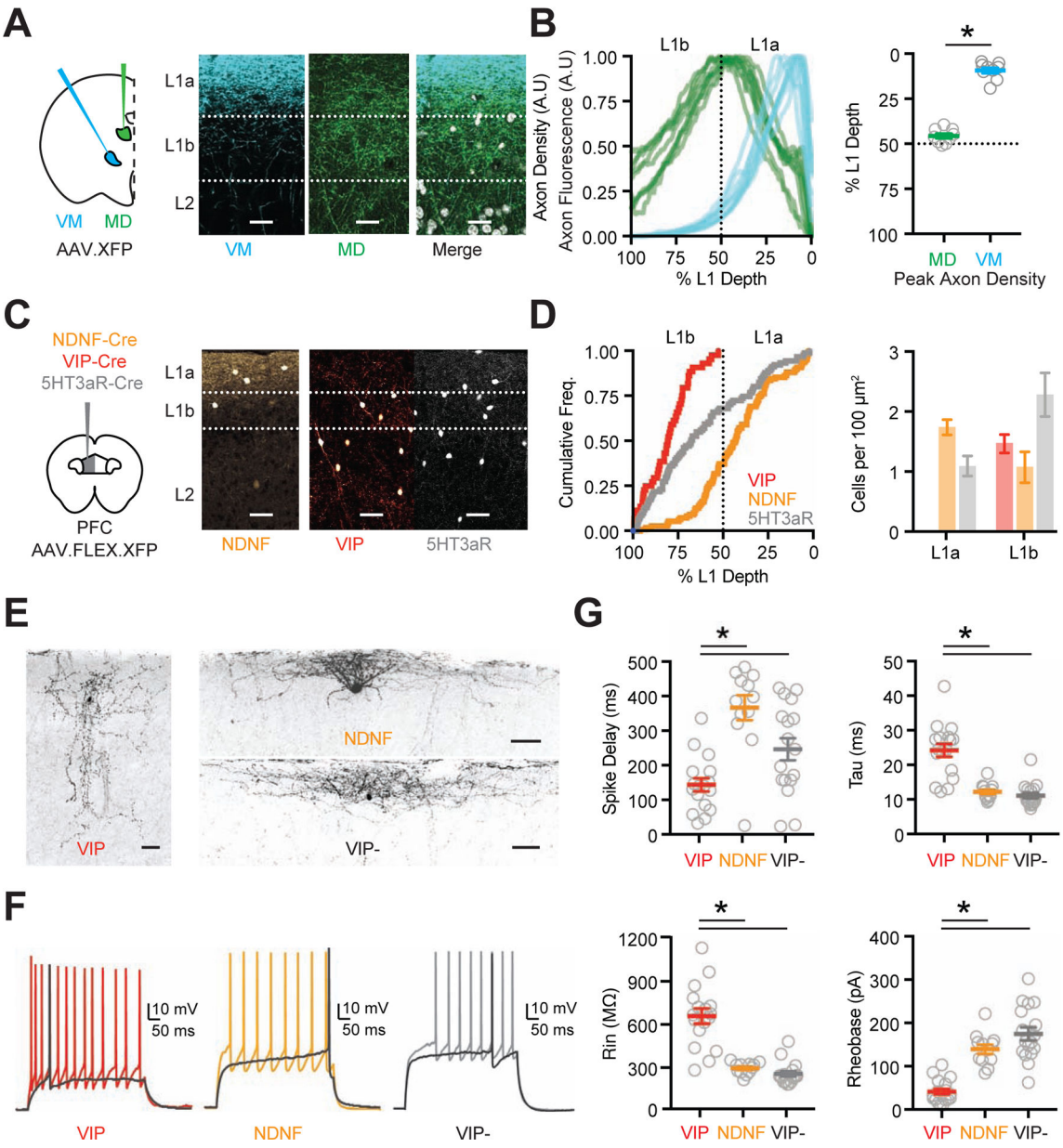

Figure 1. Thalamic axon and cortical interneurons define two L1 sublayers.

(A) Left: Schematic of AAV-XFP (either AAV-EGFP or AAV-mCherry) injections into the ventromedial (VM) and mediodorsal (MD) thalamus. Right: Representative images of superficial layers of PFC, showing VM axon (blue), MD axon (green), and merge with DAPI (grayscale). Scale bars = 25 µm.

(B) Left: Summary of axon density for VM (blue) and MD (green) as a function of L1 depth (0% is pial surface). Lines are normalized axon density plots from individual slices. Right: Summary of L1 depth at which MD and VM axon density peaks.

(C) Left: Schematic of AAV-FLEX-XFP injection into the PFC of NDNF-Cre, VIP-Cre or 5HT3aR-Cre mice. Right: Representative images of superficial layers of PFC, showing labeled NDNF+, VIP+ and 5HT3aR+ interneurons. Scale bars = 50 µm.

(D) Left: Summary of cumulative frequency of interneurons as a function of L1 depth. Right: Relative cell density for NDNF+, VIP+ and 5HT3aR+ interneurons in L1a and L1b.
(E) Biocytin-recovered morphologies of VIP+, NDNF+ and VIP− cells in L1 of PFC. Scale bars = 50 μm.
(F) Representative AP firing of L1 interneurons: VIP+ non-fast-spiking (NFS) cell, NDNF+ late-spiking (LS) cell and VIP- LS cell. Dark trace is threshold spike.
(G) Summary of intrinsic properties of L1 interneurons, showing delay to threshold spike (top left) membrane time constant, Tau (top right), input resistance (Rin, bottom left) and Rheobase (bottom right). Data points are individual cells.
Averages are mean ± SEM. * = $p < 0.05$.
See also Figure S1

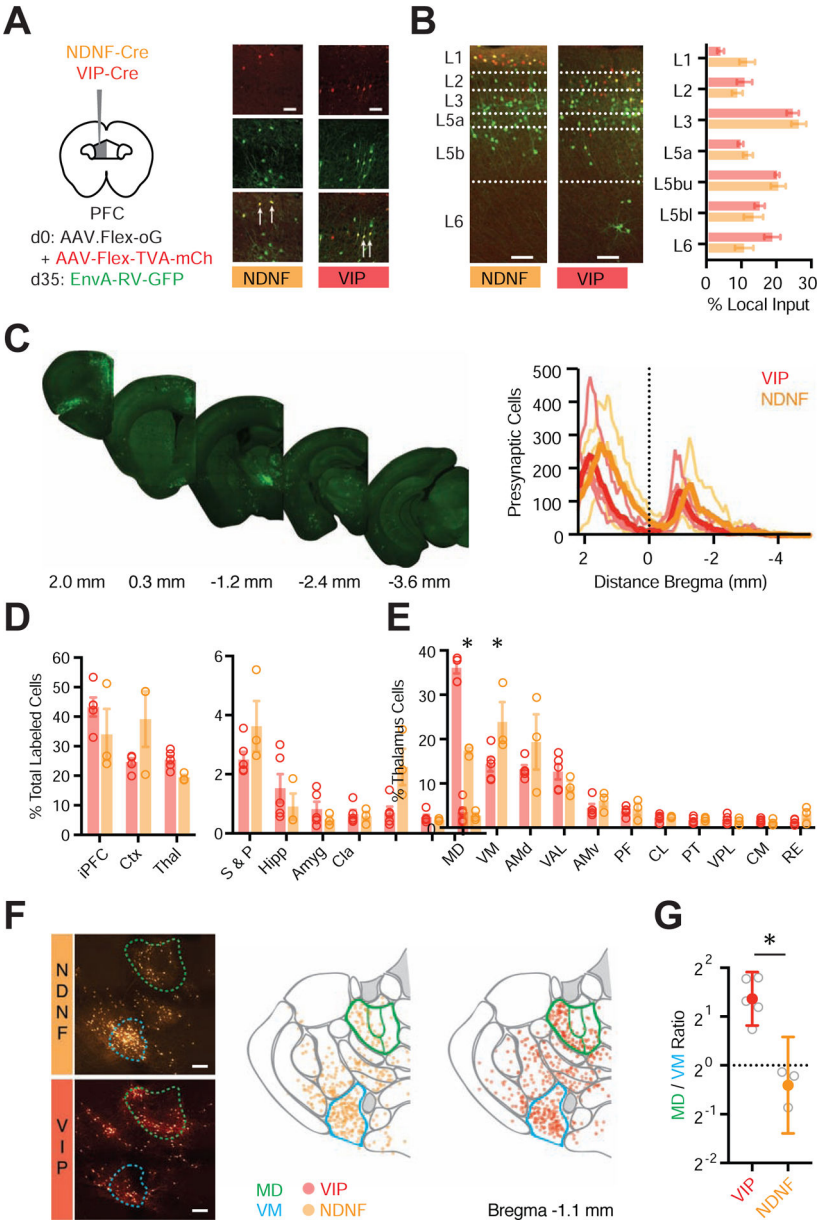

Figure 2. Brain-wide input to NDNF+ and VIP+ cells via transsynaptic rabies tracing.

(A) Left: Schematic of AAV-Flex-oG and AAV-Flex-TVA-mCherry injection into PFC of NDNF-Cre or VIP-Cre mice, followed 5 weeks later by EnvA-RV-GFP. Right: AAV-helper virus-infected cells in L1 of prelimbic PFC are labeled in red. Presynaptic cells are labeled in green. NDNF+ and VIP+ starter cells are labeled in yellow and indicated by arrows. Scale bar = 50 μm.

(B) Left: Representative images of GFP+ presynaptic cells across layers of prelimbic PFC in NDNF-Cre or VIP-Cre mice. Right: Quantification of percentage of GFP+ presynaptic cells in different layers. Dashed lines indicate layer boundaries. Scale bar = 100 μm.

(C) Left: Example images of GFP+ presynaptic cells in coronal sections relative to bregma. Right: Summary distribution of GFP+ presynaptic cells along the rostro-caudal axis, with plots for individual mice (light traces) and averages (dark trace).
(D) Summary of percentage of GFP+ presynaptic cells in different brain regions. Data points from individual mice are shown as colored circles. iPFC = ipsilateral PFC (PL, IL, and rostral component of dorsal ACC), Ctx = remainder of cortex (excluding iPFC), Thal = thalamus, S & P = striatum and pallidum, Hipp = hippocampus, Amyg = amygdala, Cla = claustrum.
(E) Summary of percentage of thalamic GFP+ presynaptic cells in different nuclei, including MD and VM. Data points from individual mice are shown as colored circles.
(F) Left: Example images of GFP+ presynaptic cells in the thalamus of NDNF-Cre (top) and VIP-Cre (bottom) mice. Middle: Location of individual cells from NDNF-Cre mice, mapped onto thalamic nuclei using the Allen brain atlas (slice 65, www.brain-map.org), where MD (green) and VM (blue) are highlighted. Right: Similar for VIP-Cre mice. Scale bar = 200 μm.
(G) Ratio of GFP+ presynaptic neurons found in MD and VM for NDNF-Cre and VIP-Cre mice. Averages are mean ± SEM (B, D, E) or geometric mean ± 95% CI (G). * = $p < 0.05$. See also Figures S2 & S3 and Tables S1 & S2

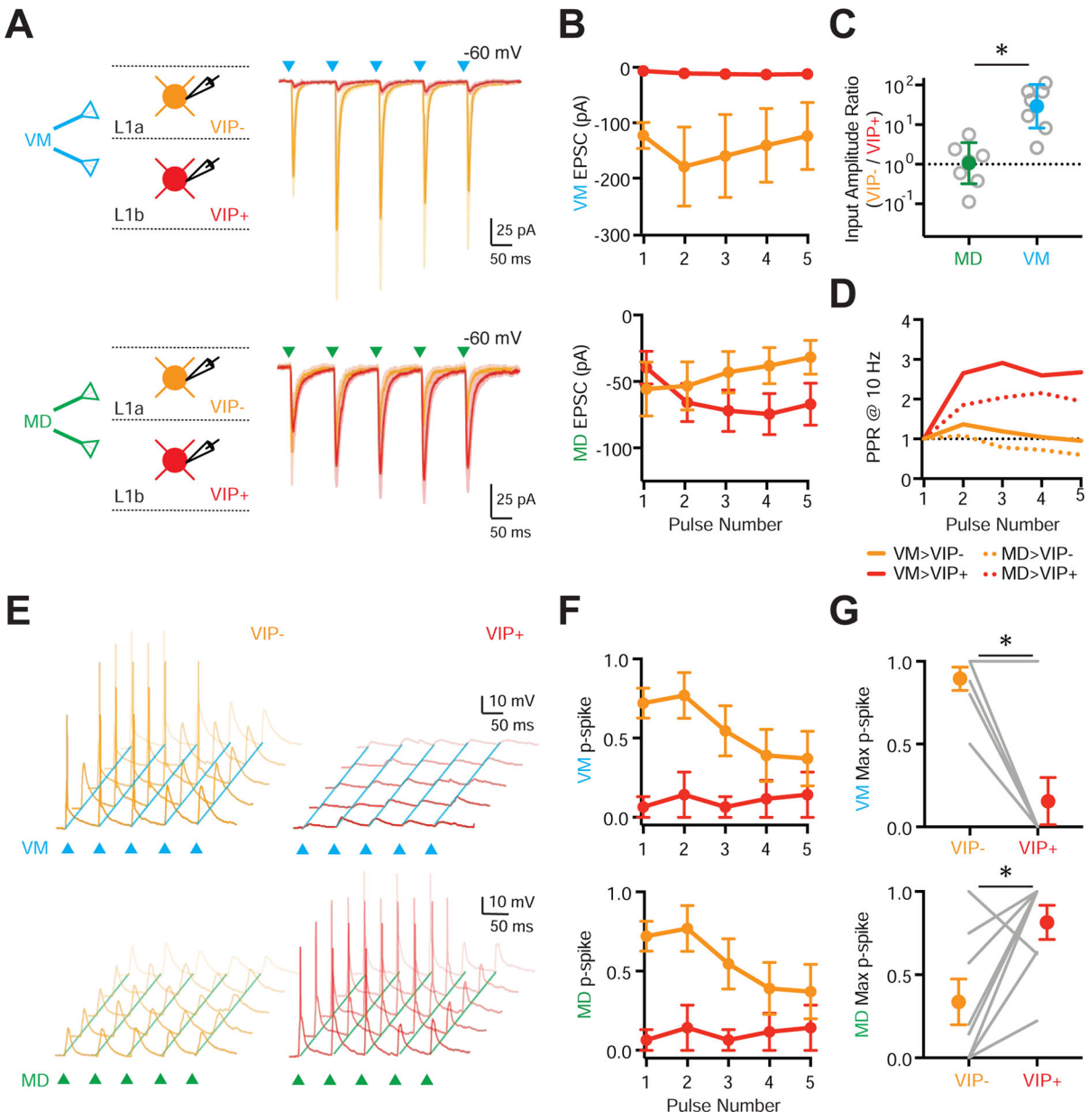

Figure 3. MD and VM differentially recruit interneuron populations in L1a and L1b.

(A) Left: Schematic for recordings of VM (top) and MD (bottom) inputs onto pairs of VIP− (equivalent to NDNF+) cells in L1a (orange) and VIP+ cells in L1b (red). Right: Average voltage-clamp recordings at −60 mV showing VM-evoked (blue triangles) and MD-evoked (green triangles) EPSCs at pairs of L1 interneurons.

(B) Summary of VM-evoked (top) and MD-evoked (bottom) EPSC amplitudes versus pulse number at pairs of L1 interneurons.

(C) Summary of (VIP− / VIP+) input ratio for first VM-evoked (blue) and MD-evoked (green) EPSC amplitude at pairs of L1 interneurons. Note the logarithmic axis.

(D) Summary of paired-pulse ratio (PPR) for VM-evoked (solid lines) and MD-evoked (dashed lines) EPSCs at VIP− and VIP+ cells.

(E) Top: Similar to (A) for VM-evoked (top) and MD-evoked (bottom) EPSPs and APs at pairs of VIP− (left) and VIP+ (right) cells in response to stimulus trains (triangles), evoked from resting membrane potential. Traces shown from representative pairs of neurons, where each panel shows five traces recorded from the same cell.
(F) Similar to (B) for AP probability (p-spike) for VM (top) and MD (bottom) stimulation.
(G) Summary of maximum VM-evoked (top) and MD-evoked (bottom) p-spike at pairs of L1 interneurons across a stimulus train. Lines represent individual pairs.
Averages are mean ± SEM (B, F, G) or geometric mean ± 95% CI (C). * = $p < 0.05$.

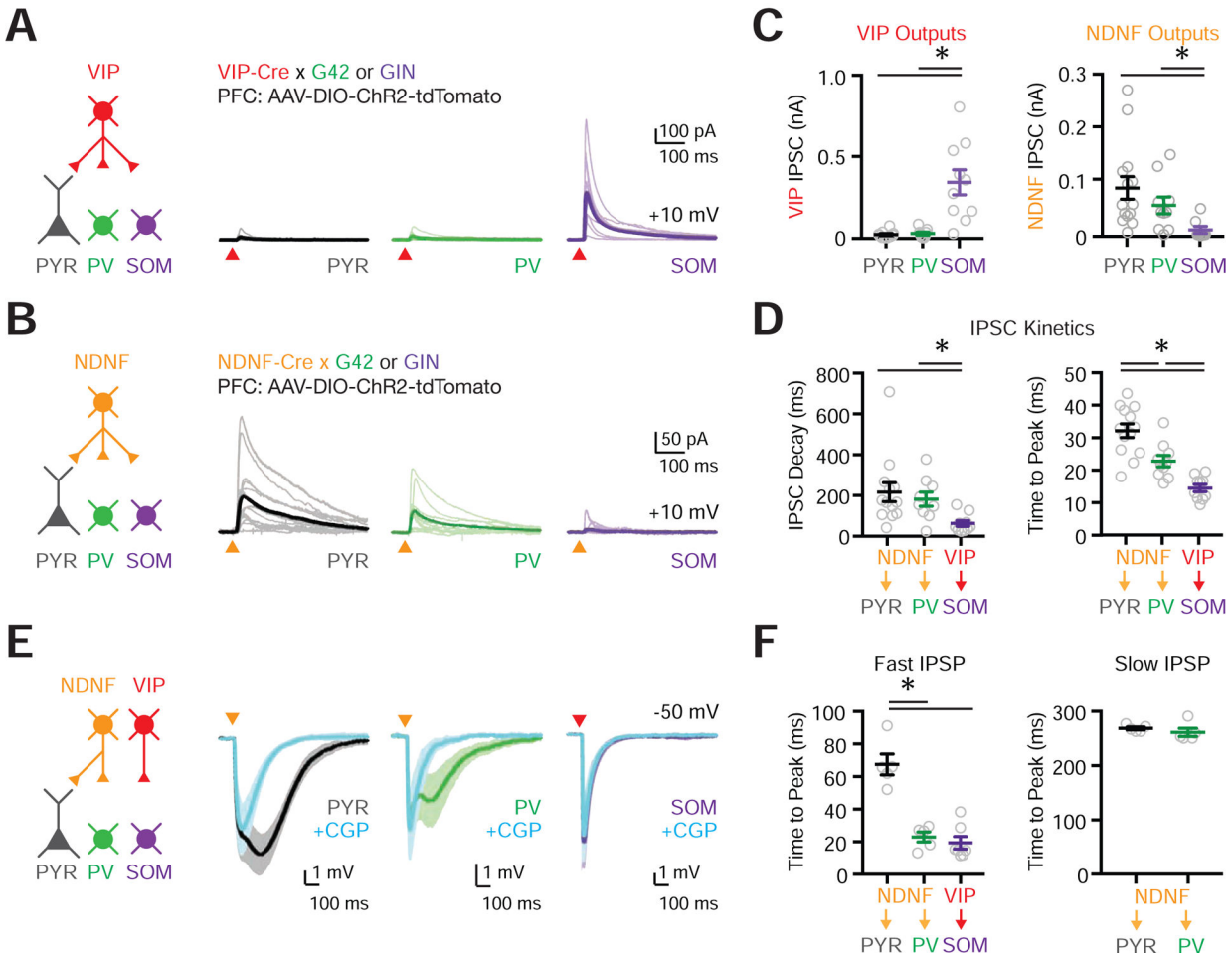

Figure 4. L1 interneurons mediate distinct inhibitory and disinhibitory pathways.

(A) Left: Schematic for studying outputs of VIP+ cells (red) onto pyramidal (PYR, black), PV+ (G42, green) and SOM+ (GIN, purple) cells in L2/3 of PFC. AAV expressing Cre-dependent ChR2 was injected into the PFC of VIP-Cre × G42 or VIP-Cre × GIN mice. Right: Voltage-clamp recordings at +10 mV showing VIP+ inputs to postsynaptic targets. Light traces are individual cells and dark traces are averages. Triangles show light stimulation.

(B) Similar to (A) but for NDNF+ connections (orange).

(C) Left: Summary of VIP+-evoked IPSC amplitude. Right: Summary of NDNF+-evoked IPSC amplitude.

(D) Left: Summary of IPSC decay kinetics for NDNF+ → PYR, NDNF+ → PV+ and VIP+ → SOM+ connections. Right: Summary of IPSC time to peak for NDNF+ → PYR, NDNF+ → PV+ and VIP+ → SOM+ connections.

(E) Left: Schematic for studying outputs from NDNF+ (orange) and VIP+ (red) cells. Right: Current-clamp recordings at −50 mV before and after bath application of the $GABA_B$-R antagonist CGP. Triangles show light stimulation.

(F) Left: Summary of the IPSP time to peak for fast NDNF- and VIP-mediated IPSPs for NDNF+ → PYR, NDNF+ → PV+ and VIP+ → SOM+ connections. Right: Similar but for slow NDNF-mediated IPSPs for NDNF+ → PYR and NDNF+ → PV+ connections.

Values are mean ± SEM (C, D, F). * = $p < 0.05$.

See alsoFigure S4

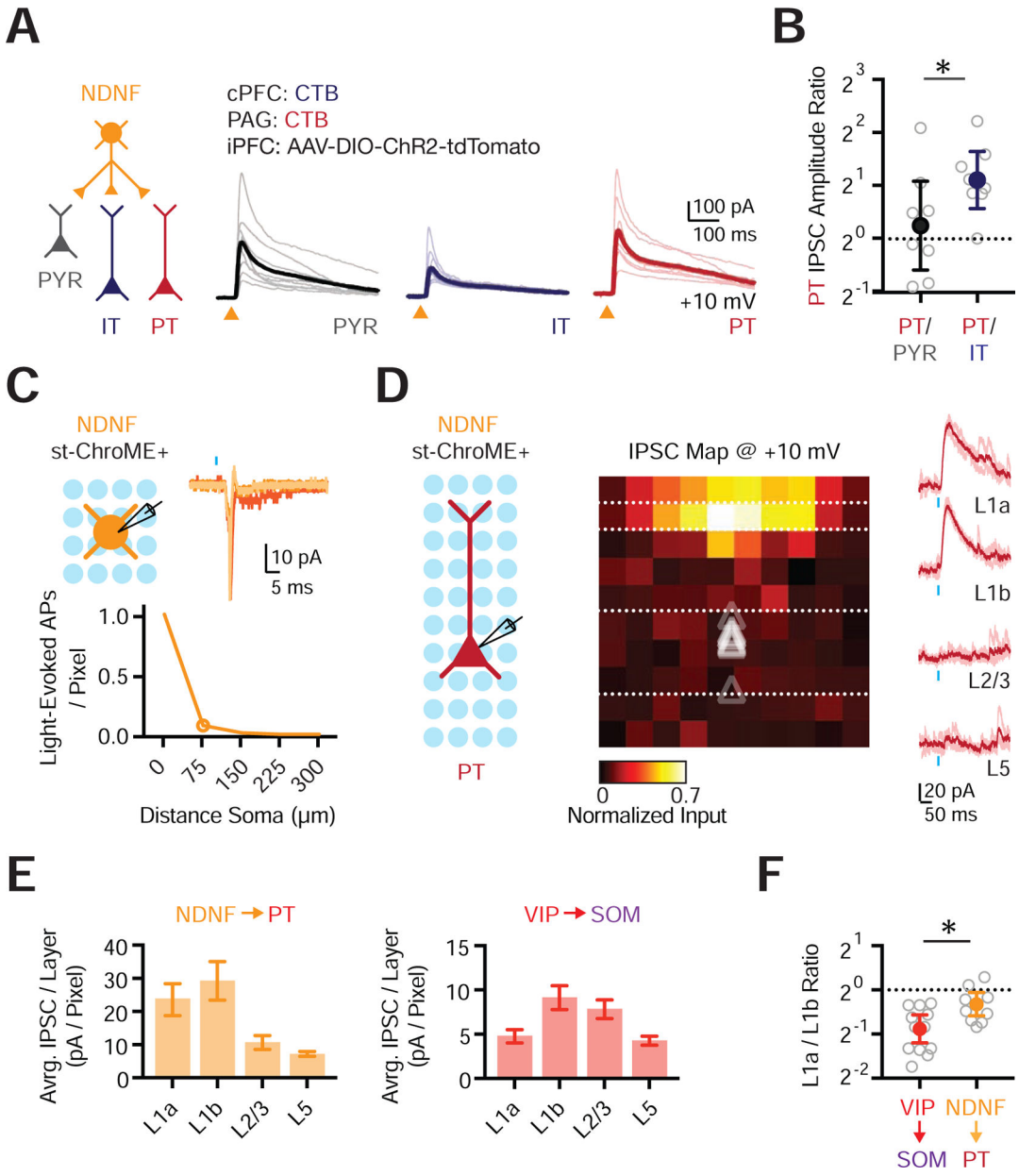

Figure 5. NDNF+ cell targeting of cortical pyramidal neuron subtypes.

(A) Left: Schematic for studying outputs from NDNF+ cells (orange) onto PYR (black), IT (blue) and PT (red) cells. Right: Voltage-clamp recordings at +10 mV showing NDNF-evoked IPSCs at the three different cell types. Light traces are individual cells and dark traces are averages. Triangles show light stimulation.

(B) Summary of IPSC amplitude ratios from recorded triplets, calculated by dividing the IPSC amplitude recorded in PT cells by the IPSC amplitude recorded in either PYR or IT cells. Note the logarithmic axis.

(C) Top left: Recording schematic, showing grid of light spots. Top right: Representative examples of light-evoked action potentials (APs) recorded in cell-attached mode from an NDNF+ st-ChroME+ cell stimulating over the soma. Blue bar shows light stimulation.

Bottom: Summary of the number of light-evoked APs per pixel as a function of distance from the soma for all NDNF+ st-ChroME+ cells recorded in cell-attached mode.
(D) Left: Recording schematic, showing grid of light spots. Middle: Normalized maps of NDNF-evoked IPSCs at PT cells, indicating location of presynaptic cells. Triangles show soma depth of recorded cells. Individual pixels are 75 × 75 μm. Right: Representative examples of NDNF-evoked IPSCs recorded in voltage-clamp at +10 mV across different layers. Light traces are individual trials and dark traces are averages. Blue bar shows light stimulation.
(E) Left: Summary of IPSC amplitude per pixel calculated by dividing the total current (in pA) per layer by the number of pixels, showing relative input strength across different layers for maps of NDNF+ connections onto PT cells. Right: Similar for VIP+ connections onto L2/3 SOM+ cells.
(F) Summary of L1a / L1b input ratio for VIP+ → SOM+ and NDNF+ → PT connectivity maps. Values are mean ± SEM (C, E) or geometric mean ± 95% CI (B, F). * = $p < 0.05$.
See also Figure S5

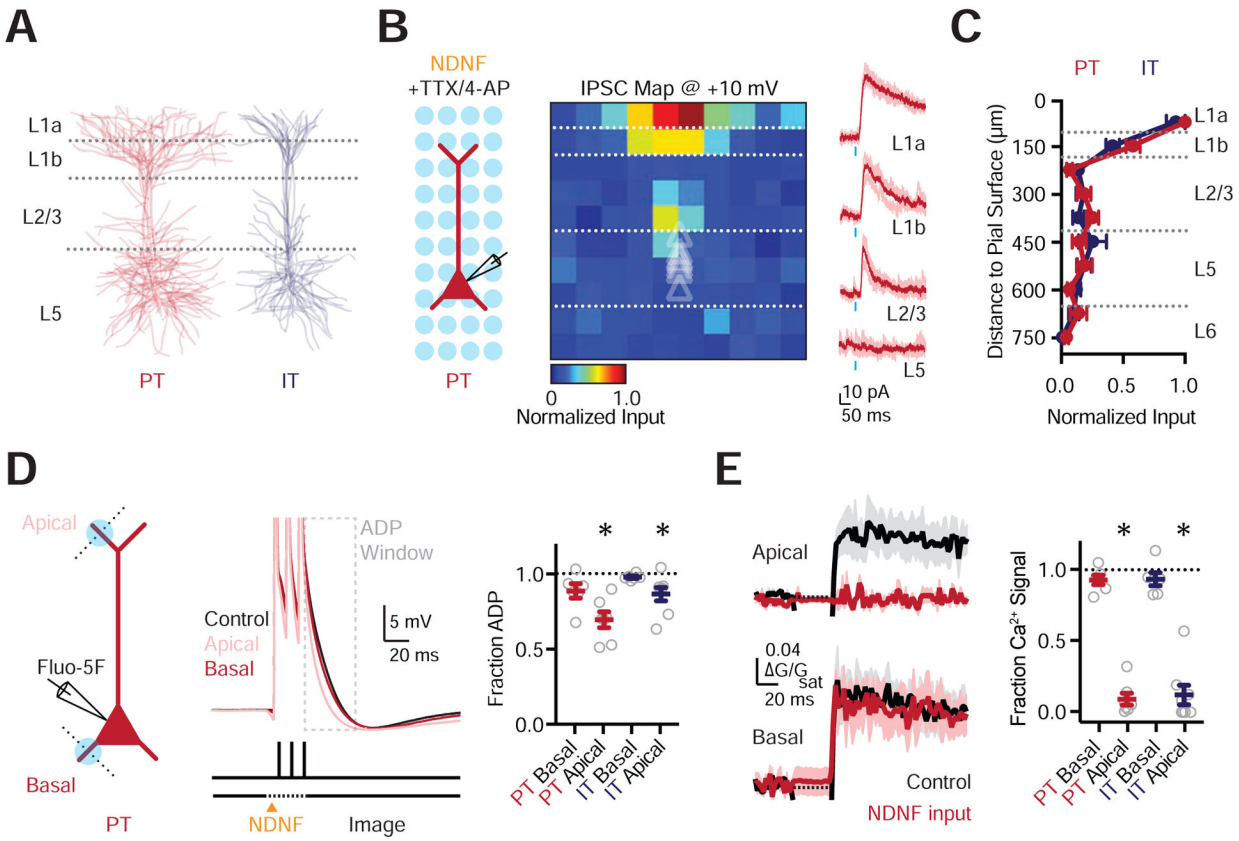

Figure 6. NDNF+ interneurons control apical dendrite electrogenesis.

(A) Morphological reconstructions of PT and IT cells, each showing 6 overlaid cells.

(B) Left: Recording schematic, showing grid of light spots. Middle: Normalized sCRACM for NDNF-evoked IPSCs onto PT cells, recorded at +10 mV in the presence of TTX and 4-AP, indicating synapse location. Triangles show soma depth of recorded cells. Individual pixels are 75 × 75 µm. Right: Representative examples of NDNF-evoked IPSCs at the different layers. Light traces are individual trials and dark traces are averages. Blue bar shows light stimulation.

(C) Summary of normalized NDNF-evoked IPSC amplitude as a function of distance to the pial surface for PT and IT cells.

(D) Left: Schematic of whole-cell recording from PT cells, 1-photon NDNF+ stimulation (blue circles), and 2-photon line-scans (dashed lines). Middle: Somatic action potentials (3 × 100Hz) paired with NDNF+ input to either the apical or basal dendrites. Grey box indicates the region of interest for ADP analysis. Right: Summary of reduction in ADP due to stimulation at the apical but not basal dendrites of PT and IT cells.

(E) Left: Corresponding AP-evoked Ca2+ signals in the apical and basal dendrites, in control conditions (black) or paired with NDNF+ stimulation (red). Right: Summary of reduction in AP-evoked Ca2+ signals due to stimulation at apical but not basal dendrites of PT and IT cells.

Values are mean ± SEM (C, D, E). * = $p < 0.05$.

See also Figure S6

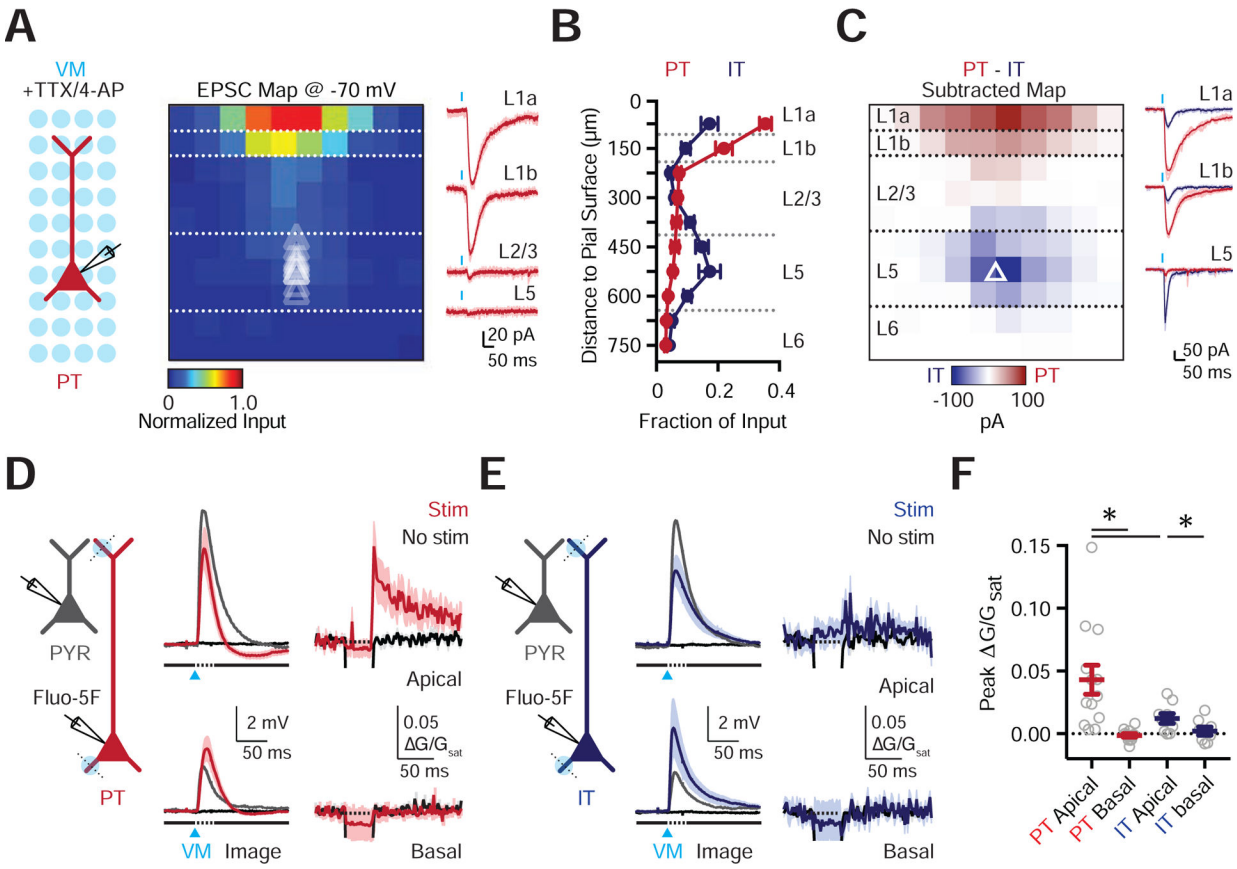

Figure 7. VM input drives apical dendrite electrogenesis in L5 PT cells.

(A) Left: Recording schematic, showing grid of light spots. Middle: Normalized sCRACM for VM-evoked EPSCs onto PT cells, recorded at −70 mV in the presence of TTX and 4-AP, indicating synapses in dendrites. Triangles show soma depth of recorded cells. Individual pixels are 75 × 75 µm. Right: Representative examples of VM-evoked EPSCs at individual layers. Light traces are individual traces and dark traces are averages. Blue bar shows light stimulation.

(B) Summary of normalized VM-evoked EPSC amplitude as a function of distance from the pial surface for PT (red) and IT (blue) cells.

(C) Left: Subtracted (PT – IT) connectivity maps. Right: Examples of VM-evoked EPSCs at different layers from a pair of PT (red) and IT (blue) cells. Examples are individual (light traces) and average response (dark traces). Blue bar shows light stimulation.

(D) Left: Schematic of recordings from PYR (grey) and PT (red) cells, 1-photon VM stimulation (blue circles), and 2-photon line scans (dashed lines). Middle: VM-evoked EPSPs at PYR (grey) and PT (red) cells, along with no stimulation (black). Right: Corresponding VM-evoked Ca2+ signals in the apical and basal dendrites of PT cells.

(E) Similar to (D) for IT cells.

(F) Summary of peak VM-evoked Ca2+ signals in the dendrites of PT and IT cells.

Values are mean ± SEM (B, F). * = $p < 0.05$.

See also Figure S7

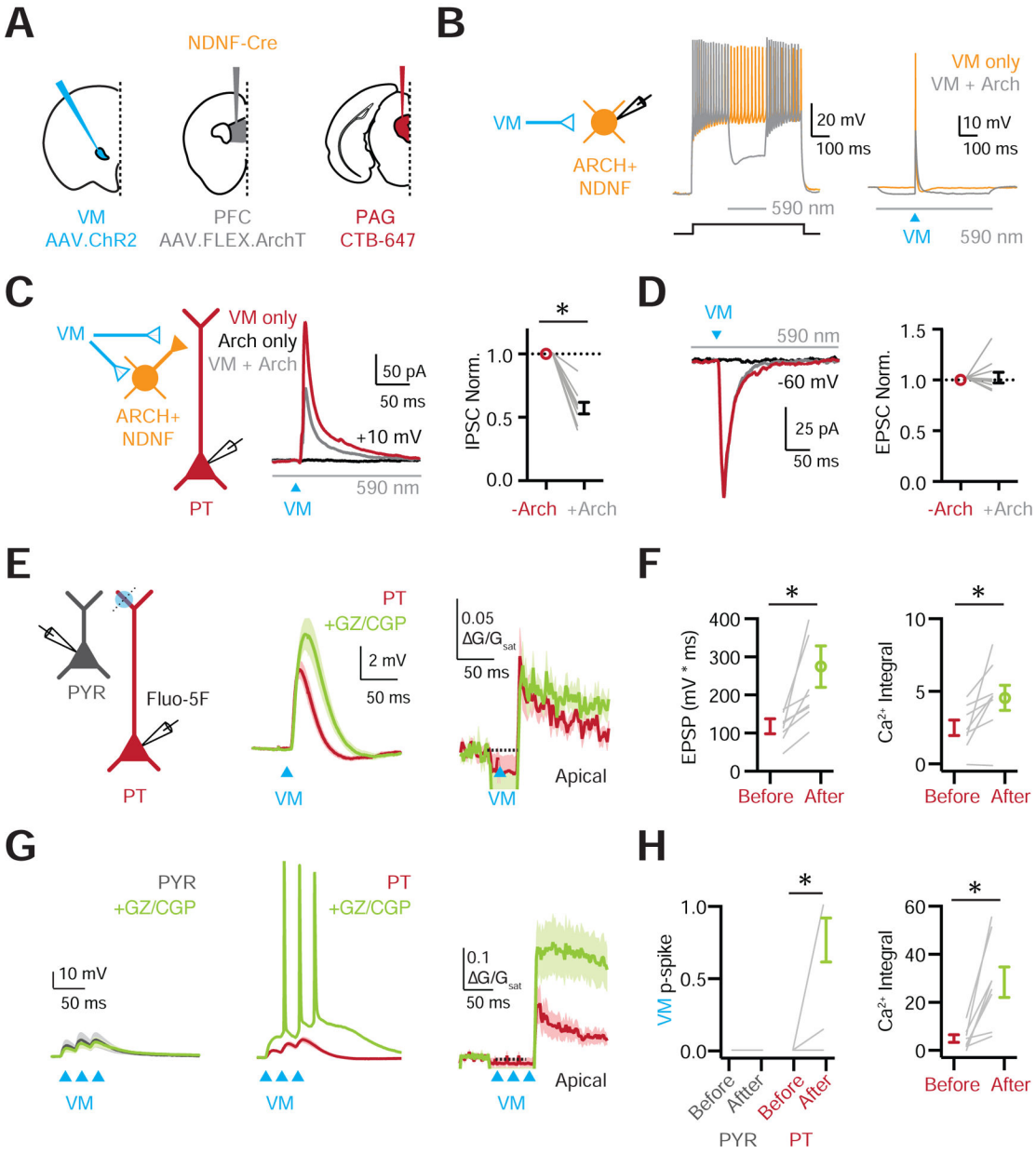

Figure 8. NDNF+ cells control PT dendritic electrogenesis and firing.

(A) Schematic of injections of AAV-ChR2 into VM, AAV-FLEX-ArchT into PFC, and CTB-647 into PAG of NDNF-Cre mice.

(B) Left: Recording schematic. Middle: NDNF+ cell firing evoked by current step in the absence (orange trace) and presence (grey trace) of yellow light to activate ArchT (590 nm, 200 ms) and hyperpolarize the NDNF+ cell. Right: Similar for VM-evoked firing with blue light to activate ChR2 (473 nm).

(C) Left: Recording schematic. Middle: VM-evoked IPSCs measured at +10 mV from PT cells, evoked with blue light to activate ChR2 in the absence (red) or presence (grey) of yellow light to activate ArchT, with black trace showing ArchT-only control. Right:

Summary of normalized VM-evoked IPSC amplitudes, without (red) and with (grey) the activation of ArchT.

(D) Similar to (C) for VM-evoked EPSCs at −60 mV, showing no effect.

(E) Left: Schematic of recordings from PYR (grey) and PT cells (red), 1-photon stimulation of VM inputs (blue circles), and 2-photon line-scans (dashed lines). Middle: VM-evoked EPSPs at PT cells before (red) and after (green) wash-in of the GABA-R antagonists GZ and CGP. Right: Corresponding VM-evoked Ca2+ signals evoked in the apical dendrites before and after GABA-R antagonists.

(F) Left: Summary of VM-evoked EPSP integral before and after GABA-R antagonists. Right: Similar for VM-evoked Ca2+ signals.

(G) Similar to (E) for trains of VM inputs (3 × 50 Hz), also showing PYR cells (grey).

(H) Left: Summary of VM-evoked firing probability in PYR (grey) and PT (red) cells before and after GABA-R antagonists. Right: Similar for VM-evoked Ca2+ signals at PT cells.

Values are mean ± SEM (C, D, F, H). * = $p < 0.05$.

See also Figure S8

KEY RESOURCES TABLE

REAGENT or RESOURCE	SOURCE	IDENTIFIER
Bacterial and Virus Strains		
AAV1-CB7-mCherry	Penn Vector Core	AV-1-PV1969
AAV1-hSyn-EGFP	Penn Vector Core	AV-1-PV1696
AAV1-CAG-FLEX-tdTomato	Penn Vector Core	AV-1-ALL864
AAV9-CAG-FLEX-EFGP	Penn Vector Core	AV-9-ALL854
AAV1-hSyn-hChR2-eYFP	Penn Vector Core	AV-1–26973P
AAV1-CAMKIIa-hChR2-mcherry	Penn Vector Core	AV-1–26975
AAV1-EF1a-DIO-hChR2-eYFP	Penn Vector Core	AV-1–20298P
AAV1-EF1a-dflox-hChR2-mCherry	Addgene	20297-AAV1
AAV9-CAG-DIO-ChronosM140E-ST-p2A-H2B-mRuby	Addgene	108912- AAV9
AAV9-FLEX-ArchT-GFP	UNC Vector Core	N/A
AAV1-EF1a-FLEX-TVA-Cherry	UNC Vector Core	N/A
AAV9-CAG-FLEX-oG	Salk	N/A
SADΔG-GFP(EnvA)	Salk	N/A
Chemicals, Peptides, and Recombinant Proteins		
Alexa Fluor 488	Thermo Fisher	Cat# A10436
Alexa Fluor 594	Thermo Fisher	Cat# A10438
Red retrobeads	Lumafluor	Cat# R170
Cholera toxin subunit B- 647	Thermo Fisher	Cat# C34778
Biocytin	Sigma-Aldrich	Cat# B1758
Streptavidin- 647	Invitrogen	Cat# S21374
Fluo-5F	Invitrogen	Cat# F14221
CPP	Tocris	Cat# 0247
ZD-7288	Tocris	Cat# 1000
TTX	Tocris	Cat# 1069
4-AP	Tocris	Cat# 0940
NBQX	Tocris	Cat# 1044
Gabazine	Tocris	Cat# 1262
TEA	Tocris	Cat# 3068
QX-314	Tocris	Cat# 2313
CGP	Tocris	Cat# 1248
ProLong Gold with DAPI	Invitrogen	Cat# P36931
VectaShield with DAPI	Vector Labs	RRID: AB_2336790
Experimental Models: Organisms/Strains		
Mouse/C57BL/6J	Jackson Lab	RRID: IMSR_JAX:000664
Mouse/NDNF-Cre	Jackson Lab	RRID: IMSR_JAX:028536
Mouse/Ai14	Jackson Lab	RRID: IMSR_JAX:007908

Author Manuscript

Author Manuscript

Author Manuscript

REAGENT or RESOURCE	SOURCE	IDENTIFIER
Mouse/VIP-Cre	Jackson Lab	RRID: IMSR_JAX: 010908
Mouse/G42	Jackson Lab	RRID: IMSR_JAX: 007677
Mouse/GIN	Jackson Lab	RRID: IMSR_JAX: 003718
Mouse/5HT3aR-Cre	GENSAT	RRID: MMRRC_036680-UCD
Software and Algorithms		
Igor Pro	WaveMetrics	RRID: SCR_000325
MATLAB	MathWorks	RRID: SCR_001622
Prism	GraphPad Software	RRID: SCR_002798
Neurolucida 360	MBF Bioscience	RRID: SCR_001775